APPLICATION OF BEAM SHAPING IN SECOND-HARMONIC GENERATION MICROSCOPY

BY

MOHAMMAD MAHFUZUL KABIR

DISSERTATION

Submitted in partial fulfillment of the requirements
for the degree of Doctor of Philosophy in Electrical and Computer Engineering
in the Graduate College of the
University of Illinois at Urbana-Champaign, 2019

Urbana, Illinois

Doctoral Committee:

Associate Professor Kimani C. Toussaint, Chair
Professor Gabriel Popescu
Professor Sanjay Patel
Assistant Professor Liang Gao

ABSTRACT

Second-harmonic generation (SHG) microscopy, based on the second-order nonlinear susceptibility, has been established as a sub-micrometer resolution, label-free optical imaging method. Due to its selectivity for non-centrosymmetric structures and inherent confocality, SHG imaging has been used to perform three-dimensional sectioning of fibrillar biological structures such as collagen fibers. Quantitative analysis of SHG images has provided information about tissues, such as fibrillar organization, that can produce deeper insight into the relation between the tissue's structure and its function. Further application of adaptive deconvolution algorithms for SHG images has allowed significant improvement in signal-to-noise ratio, revealing the underlying helical construct of collagen fibers.

Despite the versatility of this imaging technique, the light-matter interaction has largely been limited to a Gaussian illumination intensity distribution. Restructuring the focal field intensity profile through beam shaping can be useful in reducing imaging artifacts and improving quantitative image analysis. In this dissertation, two different beam shapes are explored in the context of SHG imaging. The first approach incorporates a reflective microscope objective and a Bessel-Gauss beam illumination to reduce chromatic dispersion in SHG imaging. Using well-aligned, densely populated samples of collagen fibers, the performance of the reflective objective is systemically compared with a standard glass objective. For experiments traversing ~ 1 octave in the near–infrared and visible wavelengths, a significant reduction in chromatic aberration is observed for the RO. This work highlights the potential applicability of ROs for multimodal multiphoton microscopy.

The second research work focuses on adopting a square-shaped uniform illumination profile in a widefield imaging configuration to reduce intensity-based vignetting. The uniform illumination is obtained with a flat-top beam (FTB) that provides a comparatively higher two-photon excitation signal-to-noise ratio (SNR) distribution, as well as a reduction in the number of dark areas for a rectangular imaging region of interest. Utilizing well-aligned, densely populated tendon and randomly aligned, sparsely populated breast biopsy tissue, the effects of vignetting on quantitative SHG imaging are compared for a Gaussian beam and an FTB. This work emphasizes the utility of an FTB illumination for quantitative SHG imaging of fast, dynamic biological processes.

ACKNOWLEDGMENTS

This is the most difficult and at the same time most satisfying section to write in this dissertation. I would like to start by expressing my gratitude to the almighty for the beautiful family, academic achievement and life that I have been granted. A whole contingent of people have helped me in my academic life which culminated in this doctoral program. I will start by expressing my heartfelt gratitude to my PhD advisor Professor Kimani Toussaint. His consistent encouragement from day one has persuaded me to pursue a field of research that was significantly different from anything that I have studied previously. It was a true leap of faith to train someone who is used to thermodynamics and fluid dynamics, into the domain of optics and microscopy. His mentorship and guidance have helped me chart this unknown territory for seven long years. He encouraged me to think outside the box in my research efforts and taught me to speak and write academically (I remember the difference between m-dash and n-dash!). Most importantly, he was supportive when I made the decision to start new family in the middle of an often difficult and arduous graduate program.

I also extend my gratitude to the professors and teachers at UIUC whose courses I have taken over the course of my PhD. Especially, I would like to thank Prof. Gary Eden for being my PhD academic advisor and conducting an Optical Engineering course which was one of my favorite on campus. I would also like to mention Prof. Gabriel Popescu whose course on Modern Light Microscopy has shaped most of my knowledge of optical microscopy and formed the base of my subsequent research ideas. In the same breath, I would like to mention Prof. Sanjay Patel, whose course titled Applied Parallel Programming opened up a new dimension for my subsequent image analysis endeavors. Together with Prof. Liang Gao, I would like to thank Prof. Popescu and Prof. Patel for agreeing to serve on my doctoral committee. Finally, I would like to recognize the support of Dr. Mayandi Sivaguru who initially trained me on nonlinear microscopy at the Institute of Genomic Biology at UIUC and helped me with countless hours of research discussion, sample preparation and experimentation.

Throughout my PhD life I have been intimately involved with my lab mates, be it performing research, taking courses together or hanging out. As lab manager I had the task of organizing regular lab equipment organization and group dinners where all members of my research group participated with the utmost interest. I am thankful to Tony Lau for training me in optical microscopy and introducing me to Sunny China Buffet (guilty pleasure for grad students) and Gopala Inavalli for being a research mentor and an inspiring philosopher. A special mention goes out to Woowon Lee, Emeka Okoro and Qing Ding for starting, surviving and prospering in this PhD journey together. I am also thankful to Abdul Bhuiya (my fellow countryman in the lab), Hao Chen and Brian Roxworthy for the hours of discussions related to research and otherwise. In the last year of my PhD life, I have had the privilege of knowing Hemangg Rajput whose dedication to storytelling and bodybuilding inspires me, Varun Kelkar who makes a mean spinach-lentil dish and Adriana Salazar Coariti who taught me Spanish and the value of positivity in life.

I would like to thank my family who has always been by my side throughout this difficult journey. I would like to thank my parents Saiful and Nadira, for teaching me the importance of education and guiding me towards it. I extend my gratitude to my sister Sarjan for her love and support. Finally I am deeply appreciative of the love and emotional support offered to me by my wife Shayla from day one of my doctoral journey. I can simply say, she went a long way in making me the man I am today.

TABLE OF CONTENTS

Chapter 1

INTRODUCTION

Second-harmonic generation (SHG) is a second-order nonlinear process that transforms an incident beam of light to exactly twice the incident frequency. This effect was first demonstrated by Franken et al. in 1961 [1] for a material with no center for inversion symmetry (i.e., noncentrosymmetric) with a relative conversion efficiency of $10^{-8} \sim 10^{-9}$ [2]. In later decades, the development of pulsed laser sources with comparatively shorter pulsewidth and higher peak intensity, led to the adaptation of SHG to optical microscopy where it was used to image inorganic structures that exhibited a lack of inversion symmetry and second-order nonlinear susceptibility [3, 4]. Due to the nonlinear nature of the SHG process, the emitted signal is proportional to the square of the applied laser intensity, and as such the signal is restricted to the focal volume of a focusing objective. This phenomenon provides SHG microscopy the capability of axial sectioning with sub-micrometer scale spatial resolution, and facilitated its adaptation to biological imaging. The first tissue imaging with SHG microscopy was carried out by Fine and Hansen [5] on collagen fibers which exhibit an endogenous non-centrosymmetric structure. Since then a broad range of collagen-based tissues have been imaged with a SHG microscope, including rat tail tendon [6], breast stroma [7, 8], cornea [9, 10], skin [11, 12] and ligament [13].

Based on the success of SHG microscopy for biological imaging, several approaches were taken to obtain quantitative metrics. For example, Fourier-

transform second harmonic generation imaging (FT-SHG) performs 2-dimensional (2D) [10] and 3-dimensional (3D) [14] spatial-frequency analysis to quantify the spatial organization of type I collagen fibers in biological tissues. FT-SHG has been used to identify differences between healthy and injured tendon [15], ascertain structural changes in porcine cortical bone [16] and evaluate 3D spatial organization of fibrillar collagen in rat cervix [17]. To quantify changes in collagen fiber orientation under dynamic conditions, FT-SHG analysis has been adopted to dynamic conditions [18] where a graphics processing unit (GPU) has been implemented to obtain temporal improvements in image analysis [19]. In addition, advanced deconvolution algorithms have been applied to SHG images to obtain improved restoration of the spatial resolution revealing the underlying helical structures of collagen fibrils [20].

A conventional SHG microscope system incorporates linearly or circularly polarized illumination laser fields with a fundamental Gaussian beam mode and uniform transverse phase fronts, producing a diffraction limited focal spot when focused with a high numerical aperture (NA) objective lens [21]. The generated second-harmonic signal is dependent on the phase, polarization and intensity distribution of the incident focal field. Polarization control has often been used in SHG microscopy to characterize the polarization response of collagen fibers through two-photon Mueller matrix polarimetry [22]. Phase shaping of the transverse beam profiles has also been utilized extensively in SHG imaging for enhancement of the second-harmonic signal [23]. A limited number of research studies have focused on adapting an alternative spatial intensity distribution to explore additional mechanisms of signal control and probing capabilities. In one study, an annular-shaped beam was combined with a Gaussian beam to perform subtractive SHG imaging and improve the spatial resolution by ~25% beyond the diffraction limit [24]. At the cost of reducing the penetration depth, a light sheet illumination has also been adopted to SHG imaging with the aim of increasing the image acquisition speed [25]. Other researchers have used a Bessel-Gauss beam depicting a micrometer-scale axial extent, to perform volumetric SHG imaging in a single scan

[26]. This limited body of work simultaneously highlights the opportunity of beam shaping and the dearth of exploration in that domain for SHG microscopy.

This dissertation describes the work done in exploring the avenue of focal field intensity distribution in SHG microscopy, especially in the context of quantitative analysis. The theoretical framework of the second-harmonic process is presented in Chapter 2, along with a description of an SHG imaging system and a brief overview of quantitative analysis. Chapter 3 summarizes the efforts undertaken to develop *in situ* quantitative analysis through simultaneous acquisition and analysis of SHG images. Chapter 4 explores the adaptation of a reflective mirror-based objective (RO) to perform SHG imaging with a Bessel-Gauss beam. Due to their reflection-based geometry ROs lead to a reduction in chromatic aberration, which is explored in this chapter from the context of multimodal multiphoton microscopy (MPM). Chapter 5 depicts the benefits of adopting a square-shaped flat-top beam (FTB) in a widefield illumination configuration for SHG imaging. More specifically we quantify the improved SNR and increased accuracy in quantitative SHG image analysis by incorporating a uniform illumination. Finally Chapter 6 discusses potential experimental optimization and future directions of the presented research work.

Chapter 2

BACKGROUND

2.1 Motivation

2.1.1 Collagen fibers in extracellular matrix

The extracellular matrix (ECM) is the environment surrounding cells in biological tissues. Its primary tasks involve the development of the mechanical strength, elasticity and integrity of the tissue. Proteins present in the ECM mediate cell-matrix adhesion and cell differentiation, and influence the migration patterns of cells [27]. In addition, these proteins also regulate the distribution and activation of growth factors to cells. In mammals, ~ 300 such proteins such as collagen, glycoproteins and proteoglycans [28] are involved in assembling and remodeling the ECM. More importantly, the state of the structure-function dynamics of the ECM is a key indicator of the health of the tissue or the host organ as a whole.

Among the proteins present in the ECM in mammals, collagen is the most common; in some tissues such as the bone it occupies ~90% of the ECM volume [16]. An individual collagen molecule comprises three polypeptide chains, each of which contains one or multiple amino acid motifs [29]. These motifs mostly consist of glycine, proline and hydroxyproline amino acids, which allow the collagen molecule to be formed in a triple helical structure. This sequence of amino acids is complex and non-repetitive, giving rise to a molecular structure with no inversion symmetry [6]. A typical collagen molecule is ~300 nm in length and ~1.5 nm in width. Based on structural variation, 28 different types of collagen have been

identified in humans [29]. From a biomechanical standpoint, the fibrillar forms of collagen (e.g., types I, II, III, V, XI, XXIV and XXVII) have garnered significant interest. Among them, type I collagen is the most prevalent as it is found in large quantities in bone, cornea, tendon, lung, ligament, skeletal muscle and vascular tissue [29]. Fibrillar collagen exhibits a hierarchical structure whereby individual molecules are staggered together with a periodicity of 64-67 nm to form fibrils. The thickness of fibrils falls within a range of 2-200 nm. The fibrils in turn are staggered together to form fibers (thickness 200-500 nm), and eventually fiber bundles called fascicles (thickness 1-12 μm) [30]. This hierarchical structure of fibrillar collagen is shown in Fig. 2.1.

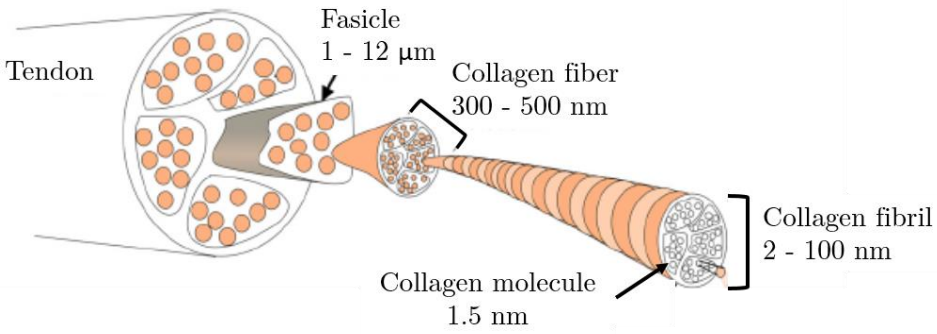

Fig. 2.1: Hierarchical structure of fibrillar collagen. Reprinted with permission from Scarr et al. [30].

Fibrillar collagen is involved in several significant biomechanical functions in the mammalian body, primarily focused towards the maintenance of mechanical strength, elasticity, stiffness and structural integrity of the constituent tissue and organs. For example, fascicles of type I collagen provide tensile strength and stiffness in tendon and define the load bearing capability, tensile strength and torsional stiffness in bones [31]. Structural anomalies or compositional variation in collagen can lead to diseases. For example, a rare genetic mutation of collagen type I has resulted in the genetic disorder osteogenesis imperfecta. This disorder has been linked to increased bone fragility, comparatively lower bone mass and several

other connective-tissue diseases [32]. Another widely prevalent condition is the corneal disorder, keratokonus, which leads to the formation of a bulge in the cornea, severely impeding the capability of the eye to focus light on the retina. This disease has been connected to a disruption in the lamellar structure of collagen fibers in the cornea [33]. These observations highlight the fact that assessment of fibrillar collagen would be valuable for a deeper understanding of its structure and function in healthy and diseased tissue. To that end, it is important to identify the necessary requirements for an imaging platform capable of capturing the structural features of collagen.

2.1.2 Imaging collagen fibers

Many microscopic imaging modalities have been used for observing collagen. Polarized light microscopy (PLM) exploits the birefringent nature of the collagen fiber to obtain a contrast mechanism. The triple-helical arrangement of the collagen molecule and the hierarchical structural arrangement of the collagen fibrils and fibers result in a uniaxial positive birefringent behavior [34]. This behavior is observed when the refractive index along the length of the fiber is higher than that obtained along the width. The birefringent nature can be lost if the helical pattern of the collagen molecule is damaged, such as due to thermal denaturation [35]. PLM operates by placing the sample between two polarizers exhibiting orthogonal polarization direction, whereby the birefringence leads to a modulation of the brightness and color of the scattered light. This modality has been used widely since the 19^{th} century to study the structural features of collagen [36, 37]. Despite the simplicity of the technique, PLM does not provide a sub-micrometer optical resolution due to its widefield illumination and image collection mechanisms [15]. The same reason also restricts the application of PLM to thin samples and 2D imaging only.

Electron microscopy has been used as an alternative to PLM to obtain images with comparatively higher resolution. Scanning electron microscopy (SEM) has

been utilized for observing the collagen organization in articular cartilage [38], whereas transmission electron microscopy (TEM) has been used for imaging the structural organization of collagen in bone to resolve the fibrillar size and structure [39]. Despite the nanometer-scale resolution, electron microscopy techniques can be damaging for biological samples and alter the internal structural organization and properties. These changes occur as the sample needs to be dehydrated for use in a vacuum environment and coated with a thin layer of metal to increase conductivity and avoid build-up of electrons. The technique of environmental SEM (ESEM) does not require dehydration or sample coating, but the procedure requires significant optimization to minimize damage to the structure of the sample [40].

Laser scanning confocal microscopy is another optical microscopy technique that has been applied in collagen imaging. In this modality, a laser beam is focused with a high numerical aperture objective lens onto the surface of the fluorescent sample. The focused beam is scanned across the surface of the sample to develop a 2D illumination pattern. The generated fluorescent signal is collected through another high NA objective lens and passed through a circular aperture to reject any signal that is not generated from the focal plane in the sample and thereby increase the spatial resolution. Finally, the photons are collected by a point detector (such as a photo multiplier tube) and a 2D image is constructed point-by-point. It has been used for imaging collagen in cardiac muscle [41], cranial vault [42] and cornea [43]. However, this method requires that the collagen content be stained with fluorescent labels which can alter the structural integrity of the tissue.

One common feature of the techniques discussed above is the lack of specificity to collagen in its molecular or fibrillar form. Even though this feature allows these techniques to be used for imaging a wider selection of structural content, it also reduces the applicability of these imaging modalities for isolating the collagen content in a tissue. To this end, SHG microscopy has a distinct advantage due to the specificity of the second-harmonic signal to the non-centrosymmetric structural arrangement observed in the fibrillar collagen. In addition to its ability to obtain

a diffraction-limited, sub-micrometer optical resolution, the specificity to collagen allows quantitative assessment of SHG images of collagenous tissues.

2.2 Second Harmonic Generation

2.2.1 Photophysics of second-harmonic generation

The second-order nonlinear optical scattering process of SHG occurs when light of a particular frequency is converted to light at double the frequency (or equivalently, half the wavelength) through interaction with a non-centrosymmetric medium. The nonlinear effect is negligible at low light intensities, but appears more noticeable at intensities on the order of 10^5 - 10^8 V/m [44]. Such high intensities require that the incident light be focused with a high numerical aperture (NA) lens, which enables the SHG to be used for 3D imaging with a sub-micrometer axial resolution. In recent times, SHG has received increasing usage as an imaging modality due to several advantages over similar nonlinear processes such as TPF. The advantages can be elucidated by comparing the photophysics of SHG with TPF. In TPF, two incident photons are simultaneously absorbed by the system to drive a fluorophore to a real excited energy state [45]. After a finite time delay (on the order of nanoseconds), a portion of this energy is lost through vibrational relaxation, and the remaining energy is radiated as a single photon (Fig. 2.2(a)) of lower energy. As energy absorption is involved, TPF leads to photon induced damage in the material and loss of coherence between the incident and radiated light. On the other hand, SHG operates through the instantaneous transition of the system to a virtual higher energy state through the interaction with two photons [1]. This process is schematically depicted in Fig. 2.2(b). These photons are instantaneously annihilated to generate a single photon of double the energy. This instantaneous process involves no molecular absorption, and as such photo-induced damage is significantly reduced, and coherence is preserved between the incident photons and the emitted SHG photon [46-48]. This particular light-matter

interaction is specific to noncentrosymmetric structural organization which enables SHG to provide endogenous contrast.

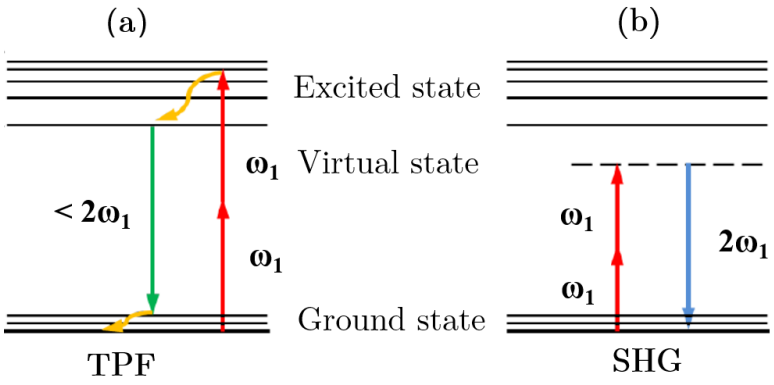

Fig. 2.2: Jablonski diagram depicting the difference between (a) TPF and (b) SHG photophysics.

2.2.2 Wave equation analysis of SHG

From a classical electromagnetic optics point of view, the origin of SHG can be understood by considering Maxwell's differential equations for a source-free medium which are given by [44, 47]

$$\nabla \times E = -\frac{\partial B}{\partial t} \tag{2.1}$$

$$\nabla \times H = -\frac{\partial D}{\partial t} \tag{2.2}$$

$$\nabla \bullet D = 0 \tag{2.3}$$

$$\nabla \bullet B = 0, \tag{2.4}$$

where E and H denote the electric and magnetic field as functions of time and space, respectively. D and B refer to the electric and magnetic flux density respectively, and they are related to the corresponding fields as

$$D = \varepsilon E = \varepsilon_o E + P \tag{2.5}$$

$$B = \mu_o H, \tag{2.6}$$

where ε_o and μ_o refer to the electric permittivity and magnetic permeability of free space, respectively. P refers to the induced polarization density that can be expressed in a power series of E as

$$P = \varepsilon_o[\chi^1 E + \chi^2 E^2 + \chi^3 E^3 + \cdots], \tag{2.7}$$

where $\chi^{(n)}$ is defined as the nth-order nonlinear susceptibility and ϵ_0 is the permittivity of free space. The first term in the equation describes the linear susceptibility $\chi^{(1)}$ which is related to the refractive index of the material through $n = \sqrt{1+\chi^{(1)}}$. The nonlinear effects are represented by the higher-order susceptibility ($n > 1$). The value of the tensor $\chi^{(n)}$ decreases dramatically with increasing n, which signifies that progressively weaker responses are observed for higher-order nonlinear processes. SHG is a second-order nonlinear process depending on the second-order susceptibility $\chi^{(2)}$. In general, second-order processes such as sum-frequency generation (SFG) and difference-frequency generation (DFG) are expressed by the second term in Eqn. 2.7 as

$$P_l(2\omega) = \sum_{m,n} \chi_{lmn} E_m\ \omega\ E_n\ \omega \qquad\qquad l,m,n = 1,2,3\ldots, \tag{2.8}$$

where ω is the angular frequency, l is the index indicating the current axis and m and n indices are used to differentiate different incident electric field. The expression for polarization density can be divided into linear and non-linear parts as

$$P = P^L + P^{NL}, \tag{2.9}$$

To obtain the wave equation for the propagation of light in a nonlinear medium, we take the curl of Eqn. (2.1) to get

$$\nabla \times \nabla \times E = -\nabla \times \frac{\partial B}{\partial t}. \tag{2.10}$$

Using vector algebra, Eqn. (2.10) can be rewritten as

$$\nabla\ \nabla \bullet E\ - \nabla^2 E = -\mu_o \frac{\partial \nabla \times H}{\partial t}. \tag{2.11}$$

Under the approximation of a slowly varying amplitude, $\nabla \bullet \mathrm{E}$ is negligible. Incorporating this observation and Eqn. (2.2) into Eqn. (2.11) results in

$$-\nabla^2 E = -\mu_o \varepsilon_o \frac{\partial^2 E}{\partial t^2} - \mu_o \frac{\partial^2 P^{(L)}}{\partial t^2} - \mu_o \frac{\partial^2 P^{(NL)}}{\partial t^2}. \tag{2.12}$$

Considering that $\mu_o \varepsilon_o = c^2$ (where *c* is the speed of light) and relative permeability ε_r is given by $\varepsilon_r = n^2$, the wave equation for nonlinear processes can be written as

$$\nabla^2 E - \frac{n^2}{c^2}\frac{\partial^2 E}{\partial t^2} = \mu_o \frac{\partial^2 P^{(NL)}}{\partial t^2}. \tag{2.13}$$

In the case of SHG the total electric field can be obtained as

$$E_p\ z,t\ = A_p e^{-j(k_p - \omega_p)t} \qquad\qquad p = 1,2. \tag{2.14}$$

In Eqn. (2.14) k_p refers to the wave vector of the fundamental (ω_1) and second-harmonic ($2\omega_1$) frequencies. Please note that the complex conjugate of the term on the right-hand side of Eqn. (2.14) has been left out due to brevity. The second-order induced polarization vector due to the three-wave mixing process is provided as [47]

$$P_2\ \omega_m + \omega_n\ = \sum_{jk}\sum_{mn} \chi_{ijk} E_j(\omega_m) E_k(\omega_n) \qquad\qquad i,j,k = 1,2,3. \tag{2.15}$$

For the degenerate case of SHG having a fixed polarization and propagation direction of the electric field, the amplitude of each frequency component can be reduced to

$$P_2\ z\ = 4d_{eff} E_1^* E_2 = 4d_{eff} A_1^* A_2 e^{-j(k_2 - k_1)z} \tag{2.16}$$

$$P_2\ z\ = 2d_{eff} E_1^* E_2 = 2d_{eff} A_1^2 e^{-2j(k_1)z}, \tag{2.17}$$

where d_{eff} is a scalar term expressing the effective value of the second-order susceptibility, A_1 and A_2 are the amplitudes of fundamental and second-harmonic electric field. The complex conjugate terms have been omitted on the right-hand side for brevity. Under the slowly varying approximation for a monochromatic source ($\left|\frac{\partial^2 A_p}{\partial z^2}\right| \ll \frac{\partial A_P}{\partial z}$) and substituting the expressions for *E* and *P* from Eqn.

(2.14) and (2.16) or (2.17), the nonlinear wave equation (2.13) can be expressed in terms of the amplitudes as

$$\frac{dA_1}{dz} = \frac{d_{eff} A_2 A_1^*}{2jk_1} e^{i(2k_1 - k_2)z}, \tag{2.18}$$

$$\text{and} \quad \frac{dA_2}{dz} = \frac{d_{eff} A_1^2}{2jk_1} e^{-i(2k_1 - k_2)z}. \tag{2.19}$$

It is assumed that all frequency components obey the nonlinear wave equation.

To obtain the intensity of the second-harmonic signal, the propagation of the fundamental light through a nonlinear medium of length *L* can be considered. Assuming that the fundamental field amplitude *A* is significantly stronger than the second-harmonic field and as such remains unchanged, the amplitude of the second-harmonic field can be obtained by integrating Eqn. (2.19) over *L* to obtain

$$A_2\ L\ = \int_0^L \frac{-d_{eff} A_1^2 \omega_2^2}{2ik_2} e^{-i\Delta k z} dz, \tag{2.20}$$

where $\Delta k = (2k_1 - k_2)$. Solving Eqn. (2.20) yields

$$A_2\ L\ = \frac{d_{eff} A_1^2 \omega_2^2}{2ik_2} e^{-\frac{i\Delta k L}{2}} sinc(\frac{\Delta k L}{2}). \tag{2.21}$$

The second-harmonic intensity can be obtained by

$$I_{SHG} = \frac{|A_1|^2}{\eta}, \tag{2.22}$$

where η is the material optical impedance given as $\eta = \sqrt{\frac{\mu_r \mu_o}{\varepsilon_r \varepsilon_o}}$. For a nonmagnetic material (for example biological matter) $\mu_r \approx 1$, which leads to the conclusion that

$$\eta \propto \frac{1}{n}. \tag{2.23}$$

Substituting Eqn. (2.23) in Eqn. (2.22), the intensity can be expressed as

$$I_{SHG} = \frac{d_{eff}^2 c^2 I_1^2 \omega_1^2 L^2}{2n_1^2 n_2} sinc^2(\frac{\Delta k L}{2}). \tag{2.24}$$

From Eqn. (2.24) it can be observed that I_{SHG} is dependent on the square of the effective second-order susceptibility d_{eff}. This means that crystalline structures having a higher d_{eff} value (for example type I collagen fiber) produce stronger

SHG signal compared to other crystalline structures. It is also observed that $I_{SHG} \propto sinc^2(\frac{\Delta kL}{2})$, where Δk is the phase mismatch factor. I_{SHG} also attains the maximum value when $\Delta k = 0$, which is a condition referred to as perfect phase matching.

2.2.3 Phase matching criteria

The importance of phase matching in SHG could be elucidated by observing the variation of the second-harmonic intensity with respect to Δk as shown in Fig. 2.3. The perfect phase matching condition $(\Delta k = 0)$ is attained when the phase difference between the fundamental and second-harmonic wave is a fixed phase relationship. From a molecular dipole picture, perfect phase matching occurs when the phases of interacting dipoles are such that the generated fields add coherently to produce a total emitted field which is proportional to the square of the number of interacting molecules. However, the refractive index of any material usually changes with frequency ($n(\omega_1) \neq n(\omega_2)$), which makes it difficult to obtain perfect phase matching with collinearly propagating light.

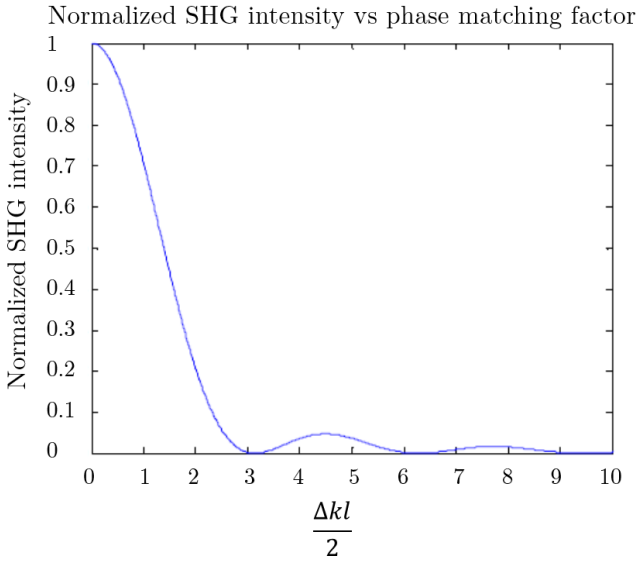

Fig. 2.3: Variation of normalized SHG intensity with respect to phase matching factor.

It is also observed from Fig. 2.3 that beyond $\Delta k = 0$ the SHG intensity varies as a sinc-squared function and non-perfect phase matching is observed. In this domain multiple localized points of maxima are observed when $\frac{\Delta k L}{2} = b\frac{\pi}{2}$, where b contains odd integers. Expanding this relation it is observed that

$$\frac{2\Delta n \omega L'}{2c} = b\frac{\pi}{2} \tag{2.25}$$

$$\frac{4\Delta n \pi L'}{2c} = b\frac{\pi}{2} \tag{2.26}$$

$$L' = b\frac{\lambda}{4\Delta n}, \qquad b = 1,3,5\ldots, \tag{2.27}$$

where L' is defined as the coherence length, which denotes the interaction length of the fundamental beam that leads to stronger SHG signal. From Eqn. (2.27) it is observed that a smaller difference in refractive index with respect to frequency is desired to increase the coherence length L', and thereby increase the SHG signal.

Owing to the difficulty in obtaining perfect phase matching, several methods have been adopted to force phase matching. In one method, the nonlinear medium is chosen to be a material with an anomalous dispersion property occurring near the absorption frequency regime of the material. This frequency is chosen such that the refractive index of the material at the fundamental and SHG frequency are equal [1, 49]. However, this approach limits the nonlinear behavior to only a small number of materials. A more widely adopted approach invokes the birefringent nature of many crystals where the refractive index property is dependent upon the fundamental beam polarization [50, 51]. In this method, the polarization of the incident light polarization is chosen along an optimal direction, and the refractive indices for the ordinary fundamental and extraordinary second-harmonic polarization can be matched for the generation of maximum second-harmonic signal. For materials possessing no birefringence (isotropic material), periodically poling the structure – either optically through the application of an external field or physically introducing periodicity during fabrication – has been used to amplify SHG [52, 53]. In this process – known as quasi phase-matching – the optical axis of the material is inverted periodically as a function of location within the material. The coupling coefficient is inverted, compensating for any phase mismatch.

In the case of biological tissues only certain tissue components such as collagen molecules are non-centrosymmetric and birefringent which makes them capable of generating a second-harmonic signal. However, appreciable SHG signal can only be observed if constructive interference of the individual SHG signals occurs. This requires that the tissue possess a sufficient density of SHG emitters and that they be ordered at the molecular level such that efficient second-harmonic signal is generated. These conditions are difficult to obtain in biological tissues due to structural variation with the tissue at various size scales [54]. Only in certain tissue components such as collagen fibers are these conditions fulfilled. In collagen fibers, periodic arrangement of SHG emitters is observed leading to a quasi-phase matching criteria with non-zero Δk values. As such, significant SHG signal is obtained when the thickness of the fiber is on the order of the SHG coherence length.

2.2.4 Symmetry requirements

A necessary requirement for second-harmonic generation is the presence of non-centrosymmetry - lack of a center of inversion symmetry - in the material structure. This requirement can be understood by observing the mechanism of SHG from a molecular dipole [55] point of view. In this picture, a centrosymmetric molecule oscillates symmetrically on being illuminated with a source of light at frequency ω. This interaction leads to light scattering in the Rayleigh regime which occurs at the same frequency. However, the interaction of the same frequency of light with a non-centrosymmetric molecule leads to an asymmetric oscillation pattern generating an additional DC (frequency of 0) and second-harmonic (2ω) component. The second-harmonic wave is known as hyper-Rayleigh scattering (HRS) and it is emitted in a dipole-like pattern. When light interacts with a regular arrangement of non-centrosymmetric molecules, the generated signals undergo constructive interference increasing the net signal output in the forward direction at the frequency of 2ω. When the net signal is strong enough to be detected by an

external detector, it is referred to as SHG. In biological matter, tissue components that contain a regular arrangement of non-centrosymmetric molecules (such as collagen fibers) are capable of SHG emission due to a coherent buildup of HRS signals. It should be noted that the constructive interference of HRS signals is only observed when the arrangement of molecules is on the order of the wavelength of incident light.

2.2.5 Emission directionality

The emitted dipole pattern of HRS and subsequently the SHG signal is strongly unidirectional, i.e., it is directed along the propagation direction of the fundamental beam. This result can be understood by considering momentum conservation requirements of the phase matching condition $\Delta k = 2k_1 - k_2 = 0$, as depicted schematically in Fig. 2.3. However, under certain circumstances appreciable backward SHG (opposite to the fundamental beam propagation) can be observed. The forward generated SHG signal can be scattered within the material leading to a portion of it being directed in the backward direction. This scattered backward SHG signal may contain multiple scattering incidents leading to loss of coherence and phase information as shown in Fig. 2.4(b). However if the scattering happens from particles separated with a periodicity of $\frac{\lambda_{SHG}}{2}$ as shown in Fig. 2.4(c), constructive interference of the backward SHG is observed and phase information is preserved. If a focused Gaussian beam is used to obtain SHG Gouy phase shift is observed at the focus of beam, which retards the incident beam in phase. This factor leads to the generated SHG to propagate at an angle to the optical axis in an effort to conserve momentum [56]. The off-axis propagation results in a backward SHG component.

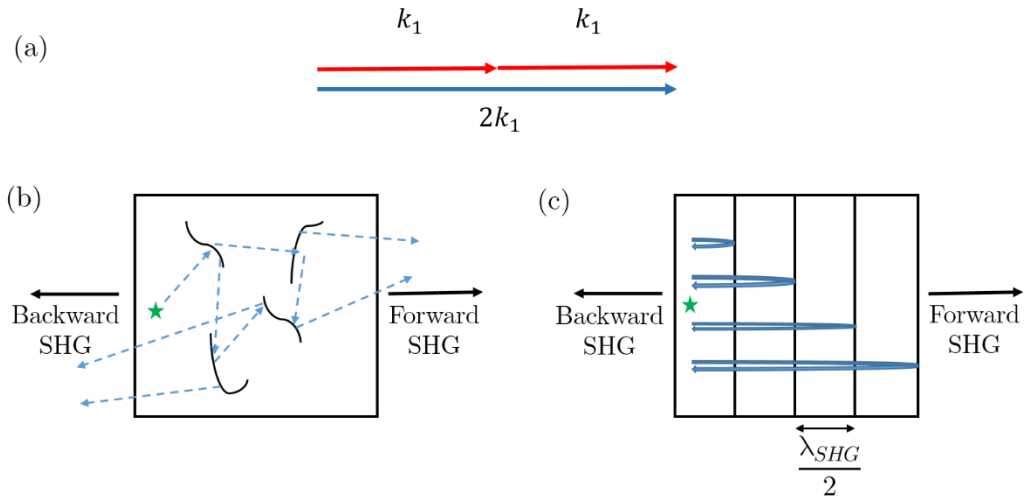

Fig. 2.4: Propagation directions in SHG. Under perfect phase matching (a) momentum is conserved leading to forward generation. Backward SHG is obtained due to scattering of the forward signal, but the locations of the scatterers determine whether the coherence is (b) lost or (c) preserved.

2.3 SHG Microscopy

The dependence of the SHG process on the second-order nonlinearity means that the generated signal is significantly weaker than the incident beam intensity and requires extremely high temporal and spatial photon density. As such, an ultrashort pulsed laser source with high instantaneous peak power and fast repetition rate is required to provide the suitable temporal photon density needed for SHG. The schematic of a typical SHG imaging setup is provided in Fig. 2.5. The laser beam is provided by a tunable (690-1050 nm) mode-locked titanium:sapphire (Ti:Saph) laser source producing 100 fs pulses at a repetition rate of 80 MHz. A standard Ti:Saph laser can provide an emission power of up to 5 W and it is optically tunable in the spectral range of 700–1000 nm, which corresponds to the range at which

biological material has comparatively lower absorption. To ensure the presence of only a Gaussian beam mode, the laser beam is spatially filtered to remove undesired laser modes. A half-wave plate and a polarizer are used in combination to maintain the polarization state of the beam and control the beam power. The standard imaging configuration involves focusing the fundamental beam into diffraction-limited spots on the surface of the sample and collecting the SHG signal point-by-point. The scanning process can be accomplished by scanning the sample or the beam through the help of galvanometer-based x-y scanning mirrors. The latter process is widely preferred due to its advantage of having comparatively faster image acquisition times for the same field of view [57]. In this method, the beam is raster scanned line-by-line on the surface of the sample. The beam is subsequently passed through a pair of scan and tube lens and reflected onto the back focal plane of a focusing objective using a short-pass beam splitter. To obtain high spatial photon crowding, a high NA objective lens is used to focus the beam to a diffraction-limited spot. SHG signal is emitted both in the forward and backward direction; here only the backward direction is shown for brevity. The SHG signal is collected with the same objective lens and passed through another short-pass filter to block any reflected laser beam. Next, the beam is optically filtered with a narrow bandpass filter to isolate the second-harmonic signal. Finally, the filtered signal is focused onto a point-detector with a tube lens. As the beam is raster scanned, SHG signal from each point in the scan is collected and used to construct a 2-dimensional (2D) image.

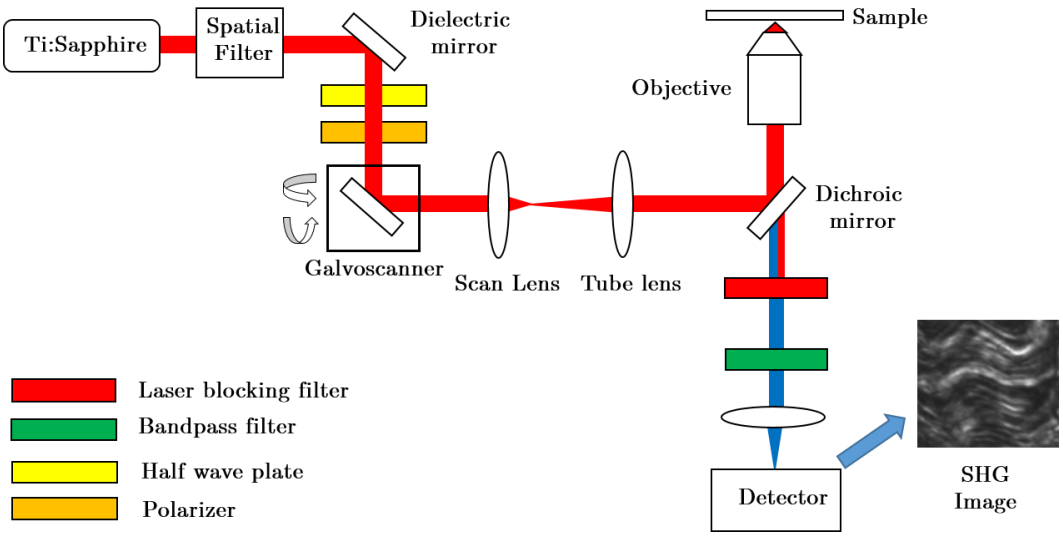

Fig. 2.5: Schematic of the optical setup for SHG microscope. In this configuration the SHG signal is collected in the backward direction.

An SHG microscopy system requires a high spatial crowding of photons to generate the second harmonic signal. In a point-scanning imaging system this phenomenon is achieved by focusing a collimated plane wave with a microscope objective. Under weak focusing conditions, i.e., when the NA of the focusing objective is less than 0.7, the focused laser beam can be approximated to be paraxial limit. In that case, the focal field intensity can be represented by [44]

$$I\ \theta\ \approx\ I_0[\frac{2J_1\ kasin\theta}{kasin\theta}]^2, \tag{2.29}$$

where I_0 is the maximum intensity, J_1 is the 0th order Bessel function of the first kind, k is the wavenumber, a is the radius of the objective aperture and θ is the focusing angle. The maximum intensity which occurs along the optical axis can be expressed as

$$I_0\ = (\frac{P_0 A}{\lambda^2 f^2})^2, \tag{2.30}$$

where P_0 is the total beam power, A represents the beam cross-sectional area, λ the wavelength and f the focal length of the lens. The intensity distribution shown in Eqn. 2.30, also known as an 'Airy disk' pattern (ADP), is a consequence of the Fourier transform of the circular aperture of the objective lens [58]. In the imaging

system, the output of an ultrafast pulsed laser source has a primarily Gaussian intensity distribution, which requires the beam to be enlarged to overfill the back focal plane of the focusing objective to provide an approximate plane wave. Figure 2.6 shows this focusing scheme, depicting the transverse and axial intensity distribution of the incident and focused beam in both 2D and 1D. Please note that ~84% of the total power of the focused beam is contained within the first bright ring of the ADP.

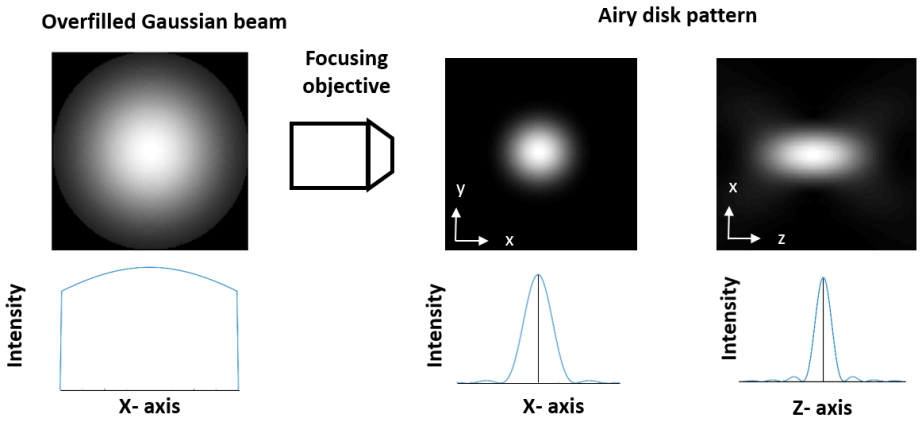

Fig. 2.6: Schematic diagram depicting the focusing mechanism used in a standard point-scanning SHG imaging system.

The spatial resolution of an SHG imaging system is constrained by the diffraction limit of the excitation wavelength and it is similar to other two-photon processes such as TPF [59]. The transverse resolution is provided by

$$w_{xy} = \frac{0.320\lambda_{exc}}{\sqrt{2}NA} \qquad NA \leq 0.7 \tag{2.31}$$

$$w_{xy} = \frac{0.325\lambda_{exc}}{\sqrt{2}NA^{0.91}} \qquad NA > 0.7, \tag{2.32}$$

while the axial resolution is provided by

$$w_z = \frac{0.532\lambda_{exc}}{\sqrt{2}}\left[\frac{1}{n-\sqrt{n^2-NA^2}}\right], \tag{2.33}$$

where n is the refractive index of the immersion medium between the focusing objective and the sample, and λ_{exc} is the wavelength of the excitation laser beam.

2.4 Quantitative Imaging of Biological Tissues

The significance of characterizing collagen-based tissue structures for assessment and diagnostic aims has motivated the development of quantitative metrics from SHG microscopy. Fourier-transform SHG (FT-SHG) is one such technique that exploits 2D [10] and 3D [14] spatial frequency analysis of SHG images to quantify structural organization of type I collagen fibers in a wide range of biological tissues at cellular scales (300 nm - 100 μm). More specifically, Fourier transform decomposes SHG images to a collection of spatial frequency values whereby the preferred orientation and angular spread in fibers can be determined by quantifying the distribution of high amplitude components. Due to its ability in differentiating structural variations in collagen-based tissues, this technique has been used to assess age-related variations in cortical bone [16], differentiate various pathological stages in stromal collagen fiber organization of human breast biopsies [8], and assess the 3D structural arrangement of collagen fibers in rat cervix [17]. In one particular case, 2D FT-SHG was used to differentiate healthy and injured horse tendon, the results of which are shown in Fig. 2.7. Using localized preferred orientation and histogram of orientation distribution, Fig. 2.7(i) depicts a well-aligned, densely packed collagen fibrillar structure for healthy, normal tendon. Application of the same methodology on SHG images of injured tendon (Fig. 2.7(ii)) showcases a comparatively lower collagen content and a wider distribution of fibrillar orientation.

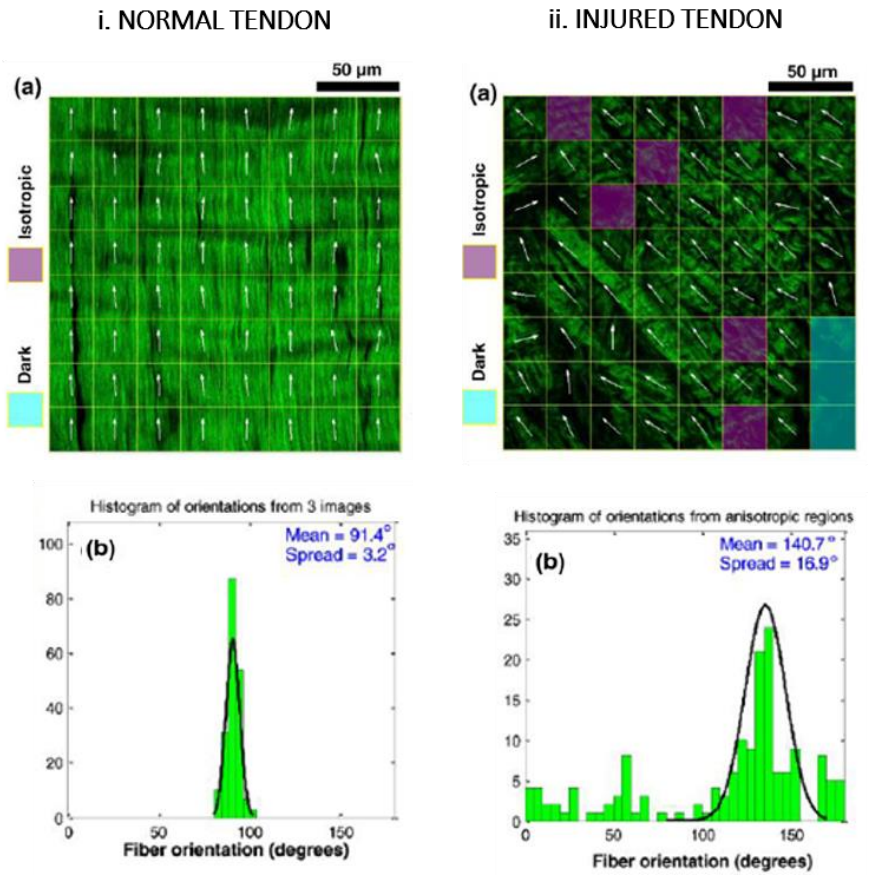

Fig. 2.7: Spatial organization showing (a) preferred orientation and (b) orientation histogram of collagen fibers from the SHG image of (1) normal tendon (2) injured tendon. Adapted from Mayandi et al. with permission [15].

The specificity of SHG imaging to collagenous tissues has led to the application of polarimetry to collagen-rich regions. Figure 2.8(i) shows one such approach, where a second-harmonic patterned polarization-analyzed reflection confocal (SPPARC) microscope uses an SHG image as an endogenous mask to identify collagen-rich regions from images obtained with reflection confocal microscopy [60]. Subsequently, linear polarimetric measures such as depolarization and linear retardance can be extracted from the resulting collagen-filtered confocal image. As shown in Fig. 2.8(ii) these metrics can be used to differentiate between the architectures of various collagenous tissues.

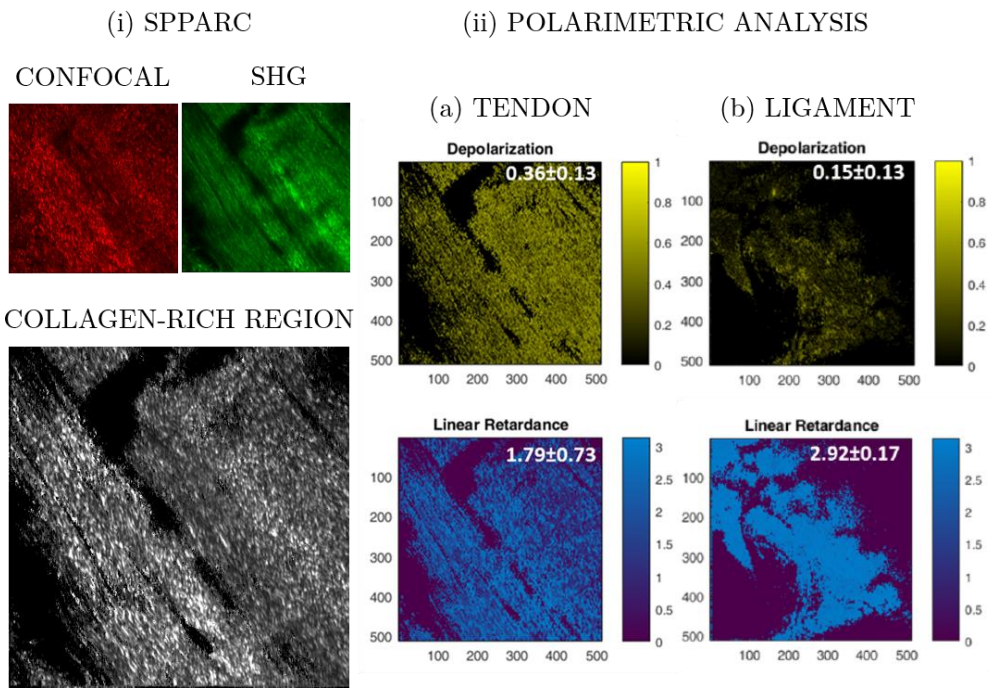

Fig. 2.8: Working principle of a (i) SPPARC microscope which uses an SHG image as a pattern to identify collagen-rich regions from images obtained with reflection confocal microscopy. This procedure allows the application of (ii) linear polarimetric analysis which can be used to differentiate collagen architecture in various tissues such as (a) tendon and (b) ligament. Adapted from Okoro et al. with permission [60]. This work was published under the creative commons license, details of which can be found in http://creativecommons.org/licenses/by/4.0/legalcode.

Chapter 3

ADAPTATION OF QUANTITATIVE SECOND-HARMONIC GENERATION MICROSCOPY FOR IN-SITU ANALYSIS

3.1 Background

The complete applicability of quantitative SHG imaging to biological problems requires the extension of such modalities to dynamic situations, which will require the image acquisition and analysis to be performed *in situ*. Simultaneous image acquisition and computing quantitative metrics of interest would be useful for an end user to change or update the imaging parameters (based on, for example, the search for collagen fibers aligned in a particular direction) during image acquisition. In addition, *in situ* image acquisition and processing could potentially lead to increased efficiency in disease detection and diagnosis by decreasing the feedback time between initial diagnosis and further action. To that end, this chapter summarizes the approaches undertaken to examine the experimental conditions required for *in situ* quantitative SHG microscopy.

3.2 Quantitative SHG Imaging under Dynamic Conditions

In an effort to identify the computational and experimental requirements for performing orientation analysis on dynamic biological processes [18], a quantitative imaging platform was developed to perform simultaneous image acquisition and orientation analysis. The image analysis time was estimated as a function of the image size, sample type and fiber density. Figure 3.1 depicts the results of the analysis, which was performed for a well-aligned, densely packed tendon sample (Fig. 3.1(a)) and a randomly oriented, sparsely distributed collagen scaffold sample (Fig. 3.1(b)). Four different imaging areas corresponding to (i) ~15x15 μm, (ii) ~30x30 μm, (iii) ~45x45 μm, and (iv) ~60x60 μm were considered. In terms of the fiber orientation analysis, the results of Fig. 3.1(a) and 3.1(b) depict that a change in the size of the imaging area does not significantly alter the results of the orientation analysis (shown below each image). As such, the circular variance is observed to be lower for tendon than scaffold for all image sizes, consistent with the fact that the scaffold showcases a more random orientation of fibers. Table 3.1 summarizes the times required to perform the orientation analysis and display the results for all SHG image sizes for both tissue types. The analysis time was observed to scale with respect to both the image size and the distribution of fibers on the image. As a result, for the same imaging area, the tendon sample required a longer analysis time compared to the sparsely distributed scaffold sample. The largest image analysis time was observed for the ~ 60x60 μm SHG image of well-aligned, densely packed tendon, which required ~ 1 s to compute and display the fiber orientation information.

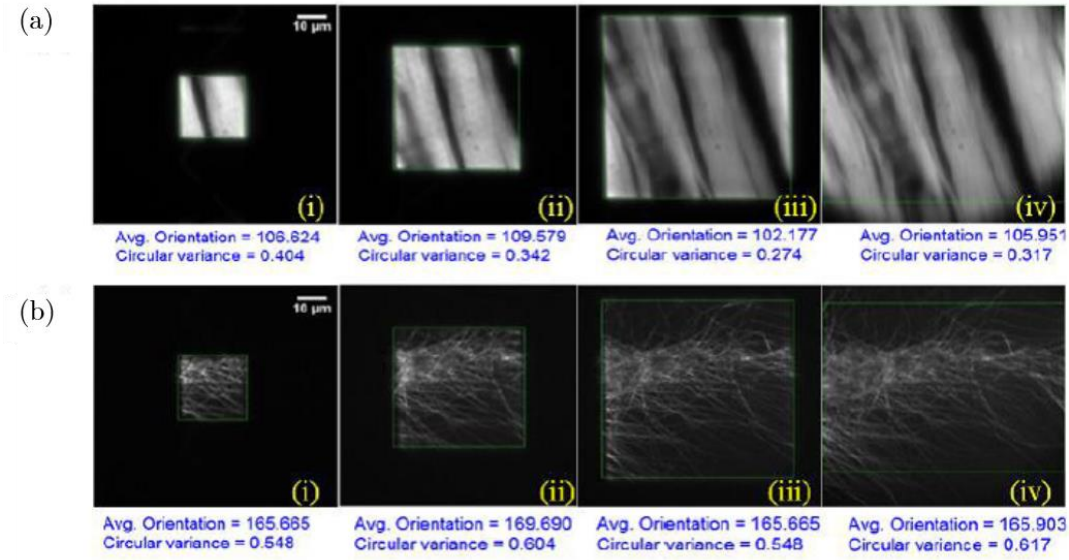

Fig. 3.1: Orientation analysis of SHG images of collagen fibers in (a) tendon and (b) scaffold. Image dimensions of (i) 15x15 µm, (ii) 30x30 µm, (iii) 45x45 µm and (iv) 60x60 µm were considered for the analysis. Adapted from Kabir et al. [18] with permission.

Table 3.1. Orientation analysis time for various SHG image sizes

Image area (µm)	Orientation analysis time (ms)	
	Scaffold	Tendon
15x15	280	420
30x30	430	570
45x45	570	680
60x60	750	950

3.3 Temporal Improvements with a Graphics Processing Unit

The simultaneous image acquisition and orientation analysis platform described in the previous section was performed using standard computer processors, whose processing speed provides a fundamental limitation on the computation time. In a subsequent study, the time required to perform orientation analysis was significantly reduced by incorporating a graphics processing unit (GPU) to the image analysis system [19]. GPUs contain multiple processing units operating in parallel whose quantity can be several thousand times more than standard computer processors. This feature has led to the incorporation of GPUs in various computational imaging applications, especially where processing time is a significant factor. For example, spectral (Fourier) domain optical coherence tomography modalities have incorporated GPU-based algorithms to reduce the computation time when compared to conventional CPU-based algorithms [61-63]. A GPU would be also useful in acquiring quantitative information at the time scales of various faster biological processes, such as the generation of an action potential in neurons [64].

For this study, a GPU-based platform was developed to perform the orientation analysis on 512x512-pixel SHG images. The images were divided into 16x16 grids, where each grid contained 32x32 pixels. The orientation analysis for each grid was computed in parallel which led to a significant reduction in overall computation time. To compute the temporal advantage, both the GPU-based and the conventional CPU-based analysis platforms were applied on consecutive frames of a video that comprised 512x512-pixel SHG images obtained from collagenous tissues showcasing a significant variation in fiber density and organization. Figure 3.2 depicts the results of analyzing consecutive frames of the video, where it was observed that GPU-based code captured and analyzed all consecutive frames while the CPU-based code performed its analysis on the first and the eleventh frames.

This result indicates a ~10x improvement in the computation time for the GPU-based orientation analysis.

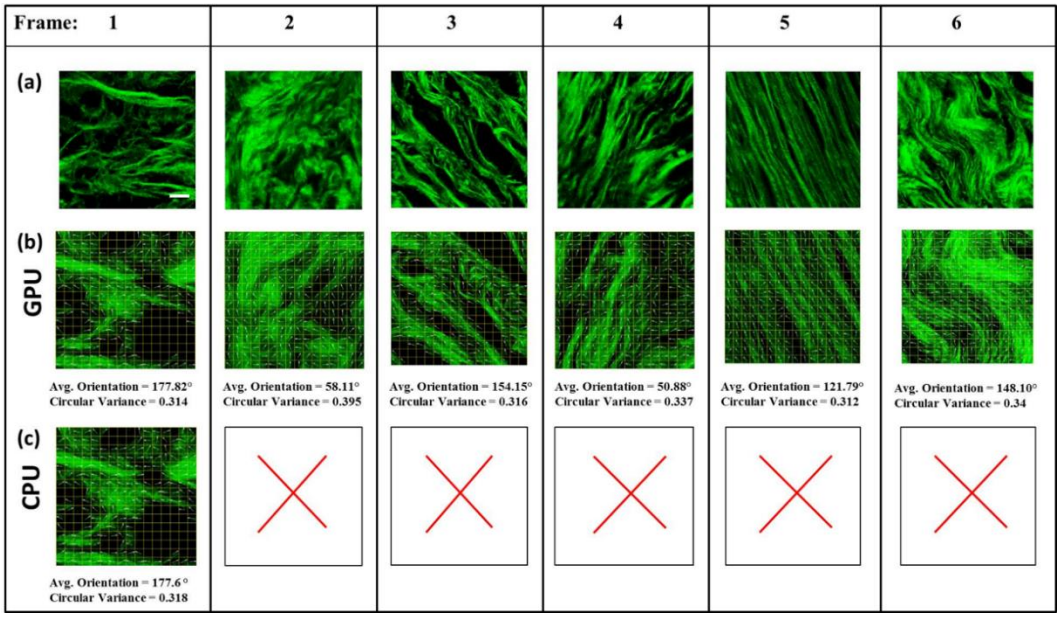

Fig. 3.2: Frames from a video of SHG images obtained from various collagenous tissues (a). Frames 1, 3, and 4 depict SHG images of human breast tissue biopsies, whereas frames 2 and 5 are of SHG images of rat cervix and porcine tendon tissues, respectively. The GPU-based code (b) successfully analyzed all consecutive frames, whereas the CPU-based code (c) was able to capture the first frame only. Adapted from Kabir et al. [19] with permission. This work was published under the creative commons license, details of which can be found in http://creativecommons.org/licenses/by/4.0/legalcode.

3.4 Application of Deconvolution for Contrast Enhancement

The accuracy of the collagen fiber orientation analysis could be improved by reducing the contribution of out-of-plane signal and restoring the resolution of the SHG process closer to its theoretical value. [57]. Image restoration techniques such as deconvolution [65, 66] can separate the desired signal from unwanted contributions in the experimental system. Deconvolution has been widely used in confocal and widefield microscopy [67, 68] to reduce the contribution of out-of-focus light in 3D images by amplifying high spatial frequencies that are associated with the image features. In a subsequent work, deconvolution was incorporated into SHG microscopy through maximum likelihood estimation along with iterative error comparison using the Richardson-Lucy algorithm [65, 66]. This method relies on an iterative convolution of a synthetically developed point spread function (PSF) and the experimentally acquired image, each iteration leading to an improved version of both the PSF and the image. The adaptive nature of this algorithm makes it useful for a scattering modality such as SHG microscopy for which it is difficult to define a PSF.

Application of the deconvolution algorithm led to significant improvement in contrast and SNR in SHG images, some of which are summarized in Fig. 3.3 [20]. Figures 3.3(a,i) and (b,i) show SHG images of tendon collagen fibers before (RAW) and after (DECONVOLVED) deconvolution. The individual collagen fibers are comparatively more distinguished in the deconvolved image, which leads to a higher resolution and contrast as depicted by Fig. 3.3(a,ii) and (b,ii). The improved contrast reveals the helical arrangement in the fibrillar architecture in collagen. As presented in Fig. 3.3 (c) and (d), the deconvolution leads to comparatively larger peak intensities (~1.8x to ~3.5x) and lower full width at half maximum (FWHM) values on average then the unprocessed image, respectively [20].

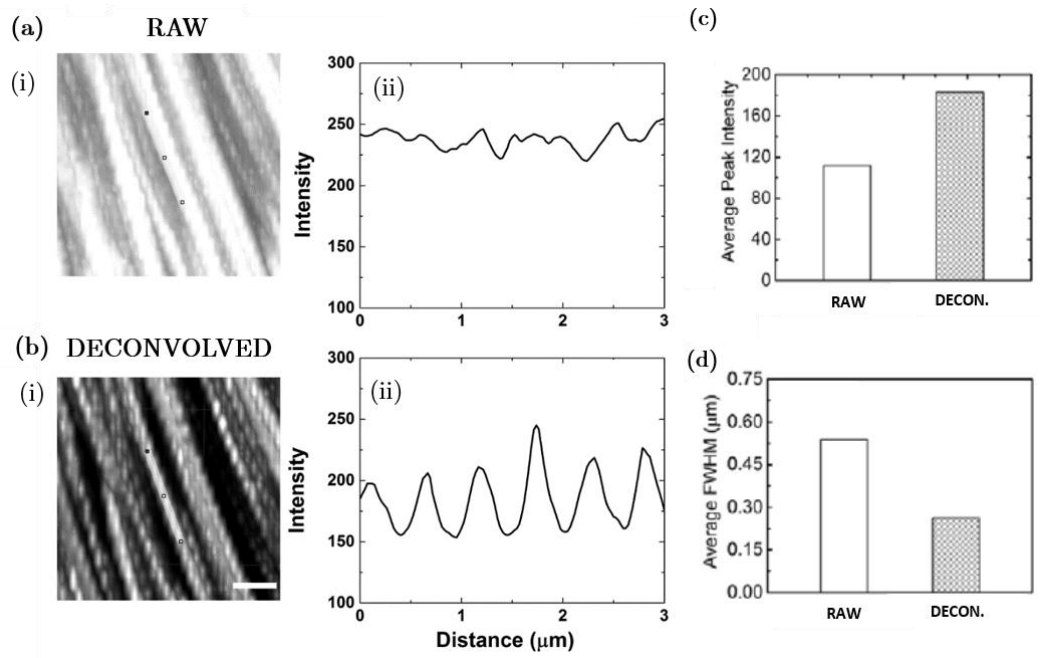

Fig. 3.3: SHG images of collagen fibers in chicken tendon (a,i) before and (b,i) after deconvolution. The helical construct of collagen fibers (chicken tendon) is clearly depicted after deconvolution. At a representative location on (a,i) and (b,i), a 3 μm long line intensity profile was drawn as shown in (a,ii) and (b,ii), depicting the pitch of the helical pattern. Increased (a) average peak intensity and decreased (b) average peak were also observed. Scale bar corresponds to 2 μm. Adapted from Sivaguru et al. [20] with permission.

3.5 Conclusion

With an aim to perform *in situ* quantitative SHG imaging, this chapter summarizes the efforts undertaken to develop a platform for simultaneous image acquisition and orientation analysis. For a ~15x15 μm SHG image of well-aligned, densely packed chicken tendon, ~1 s was required to perform orientation analysis and display the results. Subsequent incorporation of a GPU for image processing leads to ~10x improvement in the computation time. The accuracy of the orientation analysis can be increased by enhancing the SNR and contrast in SHG images

through the application of deconvolution. Adapting maximum likelihood estimation and iterative restoration, deconvolution leads to a ~3.5x enhancement of the SNR leading to visualization of the helical structure of collagen fibers with increased contrast.

Chapter 4

APPLICATION OF A REFLECTIVE MICROSCOPE OBJECTIVE FOR SHG MICROSCOPY WITH BESSEL-GAUSS BEAM ILLUMINATION

4.1 Background

The second-harmonic generation microscopy platform can be adapted for other MPM techniques such as two-photon fluorescence (TPF). This capability would allow the application of different MPM imaging platforms on the same location in a sample, each capable of identifying different structural features. In a conventional MPM setup, near-infrared (NIR) or mid-infrared laser beams are used to generate output beams that are blue-shifted by several hundred nanometers. Hence, a microscopy systems traditionally constructed with lens-based refractive optics can suffer from dispersion, which prevents different wavelengths from focusing at the same spot. Even though standard glass-based microscope objectives (SO) can be optically corrected for chromatic aberration (at an increased cost), the corrections usually apply for limited spectral bandwidths only. These bandwidths are typically observed at the illumination (e.g. 700–1100 nm) or the detection region (e.g. 350–

650 nm), which makes it challenging for multimodal MPM applications [69]. Reflective objectives (ROs) showcasing an inverse-Cassegrain design [70] utilize curved reflective mirrors to focus light and provide an invariant focal position over a broad spectral bandwidth [71, 72]. In MPM modalities, ROs have replaced standard refractive objectives (SOs) to combine beams whose wavelengths are separated by several hundred nanometers [73, 74]. In one particular case of sum-frequency generation microscopy, an RO was used to collinearly focus laser beams of wavelengths 775 nm and 3.39 µm, leading to sum-frequency signals between 625 and 650 nm [73]. Other researchers have customized the inverse-Cassegrain design [75-77] and built all-reflective microscopy systems [78] to improve fluorescence collection efficiency and simultaneously utilize multiple illumination wavelengths for MPM imaging, respectively.

The inverse-Cassegrain design of conventional ROs requires an annular shaped incident beam at the entrance of the objective. This requirement leads to a Bessel-Gauss (B-G) beam illumination at the focus of an RO. B-G beams define a class of beams first presented by Durnin et al. in 1987 which describe certain solutions of the Helmholtz wave equation of the Bessel type [79]. A B-G beam exhibits an invariant intensity distribution along its direction of propagation, theoretically extending to infinity. In MPM modalities, a B-G beam has been adopted in TPF microscopy [80, 81] to increase the speed of volumetric imaging and form stereoscopic images.

Due to the capability of ROs to reduce chromatic aberration a systematic comparison of the performance of ROs and SOs in a multimodal MPM imaging framework would help researchers in making a suitable choice of illumination optics based on their application. Even though manufacturers of ROs occasionally provide technical information, it is restricted to a Gaussian beam illumination and linear (single-photon) microscopy applications. In this work, the optical performance of a 0.5 NA RO is compared to that of a similar SO for MPM applications. In particular, the conditions under which ROs would be effective for TPF and SHG imaging are discussed. We begin our study by modeling the illumination and two-photon

behavior of the RO for an annular illumination. Next, we compare experimental point-spread functions (PSFs) for both objectives using TPF obtained at two different illumination wavelengths (780 and 950 nm) and a single emission wavelength (530 nm). Subsequently, we examine unstained tissue SHG images obtained with the two same illumination wavelengths. Finally, we discuss the limitations of the RO in the framework of MPM imaging.

4.2 Methods

4.2.1 Sample preparation

Fluorescent beads and porcine tendon were used in this study. Fluorescent microsphere beads of 290 nm diameter were purchased from ThemoFisher Scientific. Initially, the particle concentration was 1.05 g/cm^3 which was diluted with distilled water to obtain a solution of ratio 1:1000. Subsequently, 10 ml of this solution was placed over a microscope cover slip (#1.5) and allowed to dry in ambient temperature.

Porcine tendon was collected from a local abattoir and frozen at -10 °C. To prepare the imaging sample, they were placed in Tissue Tek Cryomolds and filled with optical cutting temperature (OCT) compound. This solution was later frozen with liquid nitrogen. For SHG imaging, sections of 25 µm thickness were cut using a Leica CM3050 cryostat. Afterwards, these sections were washed with 1x phosphate buffered saline (PBS) solution to remove the OCT compound and placed on a sterilized microscope slide to dry.

4.2.2 Mathematical formulation of B-G beam

The electric field of an ideal Bessel beam can be defined as [79]

$$E\ r,z\ = J_0(kr\ \sin(\beta))\exp(ikz\ \cos(\beta)), \tag{4.1}$$

where J_0 is the Bessel function of the zeroth order and first kind, r is the distance along the plane orthogonal to the optical axis, z is the distance along the propagation axis, k is the wave vector and β refers to the angle between the wave vector k and optical axis. Because an ideal Bessel beam would carry infinite energy along its axial extent it is impossible to generate one. However, the Fourier transform of an ideal Bessel beam leads to an infinitesimally thin ring [82], which is exploited experimentally to generate approximate Bessel-Gauss (B-G) beams through the Fourier transform of annular-shaped beams. The intensity distribution near the optical axis for such beams can be expressed as [83]

$$I\ r, z\ \propto \frac{4\pi^2\beta^2 z}{\lambda}\exp(\frac{-2z^2}{z_{max}^2})J_0^2(\frac{2.4048r}{r_0}), \tag{4.2}$$

where $z_{max} = \frac{\omega_0 \cos\beta}{\sin\beta}$ and $r_0 = \frac{2.4048}{k\ \sin(\beta)}$ are the axial and lateral extents of the beam obtained at FWHM location of the B-G beam's intensity distribution.

4.2.3 Experimental setup and optical simulation

Figure 4.1(a) depicts the custom-built optical setup used for this study. Both TPF and SHG imaging experiments were performed with a titanium:sapphire pulsed laser (Spectra-Physics Mai-Tai HP) source, producing a Gaussian beam with 100 fs pulses at a repetition rate of 80 MHz. The laser is spectrally tunable between 690 and 1050 nm and the excitation wavelengths for this study are spectrally centered at 780 nm and 950 nm. A half-wave plate and a polarizer are used in combination to control the input beam power. Two axicon lenses with apex angle of 2° (AX252–B, Thorlabs) are used to transform the Gaussian beam from the laser to a collimated annular beam [84, 85]. A pair of scanning mirrors (GVS012, Thorlabs) raster scans the beam over a desired rectangular area of the sample. The beam is passed through a 4-f system consisting of two lenses (f1= 15 cm, f2 = 40 cm) that magnify and collimate the beam to fit the back aperture of the objective. The scanned beam is reflected by a short pass, 670 nm dichroic beam splitter and subsequently focused onto the sample by a 0.5 NA, 40x reflective objective

(Thorlabs LMM-40X-UVV) or a 0.55 NA, 40x standard glass objective (Carl Zeiss Microscopy LD A-Plan 40x/0.55 M27). Both TPF and SHG are collected in the backward direction through the same objective and passed through a laser-blocking filter (Semrock FF01-680/sp-25) and a suitable bandpass filter (Semrock FF01-530/40-25 for TPF, Semrock FF01-390/18-25 for SHG). The signal emitted from the sample is detected with a photomultiplier tube (Hamamatsu) and reconstructed into a 2D image.

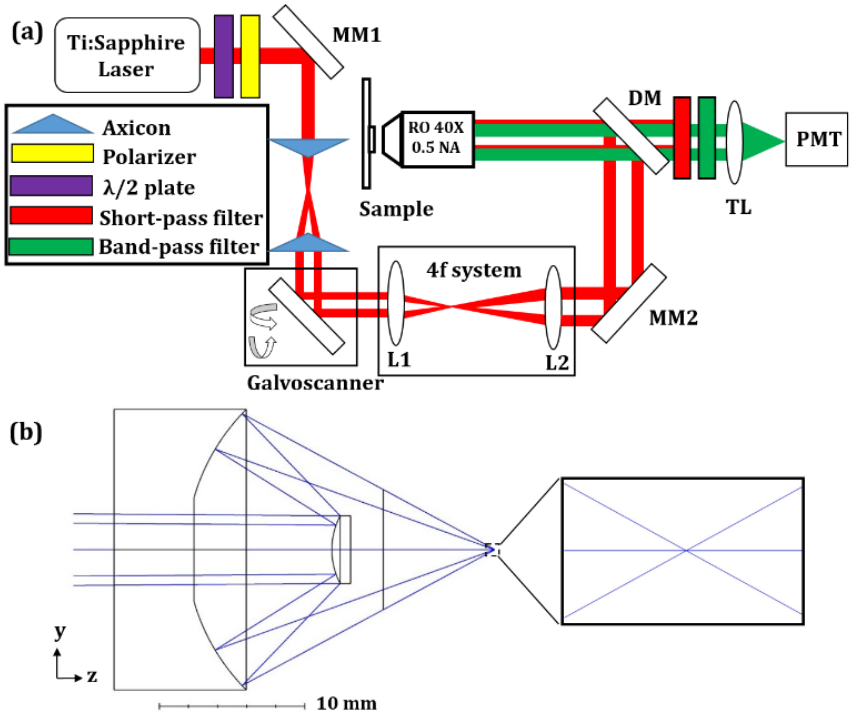

Fig. 4.1. Schematic diagram of the experimental setup showing the (a) modified MPM setup with an annular beam illumination and the results of (b) ray tracing of an annular beam through the RO. Accompanying zoomed-in view (inset in (b)) showcases rays at focus in the range of 350-950 nm wavelength of the incident light. The rays corresponding to all wavelengths overlap forming single ray lines. SM1 and SM2: spherical metal mirrors, MM1 and MM2: metal mirrors, L1 and L2: lenses, TL: tube lens, PMT: photomultiplier tube, DM: dichroic mirror. Adapted from Kabir et al. with permission [86].

Figure 4.1(b) presents the results of ray tracing of an annular beam through the RO using OpticStudio (Zemax LLC, Washington, USA) to observe the focusing of wavelengths ranging from 350 to 950 nm. From the extended view of the focal spot [inset, Fig. 4.1(b)] we observe a negligible spread in focus from 350 to 950 nm. Please note that the focal length of the RO is 5 mm. We further simulate the transverse and axial illumination PSFs created by the RO with 780 nm wavelength light, the results of which are shown in Fig. 4.2(a,i) and (a,ii), respectively. Compared to a focused Gaussian beam, the results of this simulation show a higher distribution of power in the diffraction rings and an extended axial extent for the annular illumination [26]. From the accompanying 1D intensity profiles [see inset of Fig. 4.2(a,i and ii)], the lateral (x-axis) and axial (z-axis) FWHM values are calculated to be ~850 nm and 15 µm, respectively.

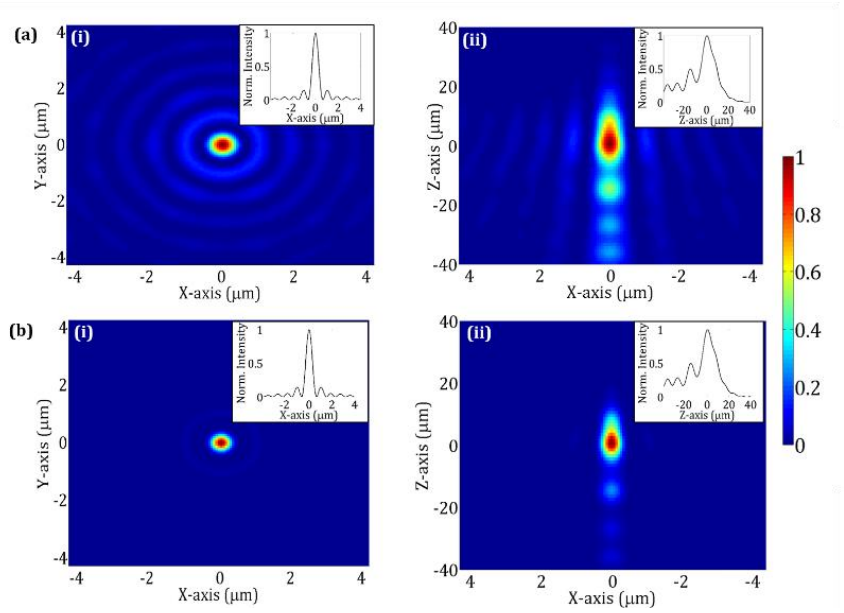

Fig 4.2: Intensity distribution after focusing through the RO. Simulated (a) illumination and (b) two-photon PSF showing (i) transverse (x-y) and (ii) axial (z) intensity distributions obtained by focusing an annular beam with a reflective objective. For each case, the intensity values have been normalized with respect to the maximum intensity. Insets in all cases show the corresponding line intensity profiles. See text for details. Adapted from Kabir et al. with permission [86].

4.3 Results and Discussion

We begin our analysis by simulating the two-photon response from the RO and calculating the transverse (x-y) and axial (y-z) two-photon PSF with an annular illumination. The results of this analysis are shown in Fig. 4.2(b). From Fig. 4.2(b,i), we observe that,~ 96% of the total intensity is contained within the central bright region at the focal plane, which strengthens the usefulness of the RO for multiphoton processes. An asymmetric distribution in the axial PSF [Fig. (4.2b,ii)] is also observed which can be attributed to the two-photon PSF of a B-G beam [80]. The power throughput of the RO is calculated by measuring the power at the entrance and exit of the objective. It is observed that, a significant portion of the illumination beam power (~40%) from the central area of the beam is reflected back when using a plane-wave illumination for the RO. However, the power throughput is substantially improved if an annular-shaped beam is adopted (<10% reflection). As such, the annular-shaped beam is chosen for the RO in this simulation and all subsequent experiments.

Next, the experimental TPF PSF of the RO and SO are measured using 290 nm diameter sub-diffraction fluorescent beads, the results of which are summarized in Fig. 4.3. A Gaussian and an annular illumination are considered for the SO as shown in columns (a) and (b), whereas only annular illumination is used for the RO (c). Illumination wavelengths of 780 and 950 nm are used in this experiment as shown in rows (i) and (ii), respectively. The objective is focused for 780-nm illumination, and the TPF images are collected using that focal plane as reference. TPF images with 950 nm illumination are collected without changing the plane of focus. In all cases 530 nm is used as the emission wavelength. For each image, the experimental PSF is obtained by measuring the FWHM from the line intensity profiles obtained across two perpendicular dashed yellow lines [Fig. 4.3(a,i)] and calculating the average. For each bead, the line intensity profile obtained along the x-axis [horizontal yellow line in Fig. 4.3(a,i)] is shown below the image of the bead. The complete procedure is repeated for 4 beads and the average PSF and standard deviation are calculated as shown in columns 2 and 3 of Table 4.1. Next, the

percentage difference between the PSF values (%Δ PSF) for all beads with 780 and 950 nm illumination is calculated. The average and standard deviation in calculated %Δ PSF values is shown in column 4 of Table 4.1. From these results, a more rapid defocusing with the Gaussian illumination is observed leading to 42.62 ± 7.01% difference in the experimental PSFs, whereas the annular illumination provides 26.14 ± 4.08% difference. In addition, relative to the middle plane of the bead, which has the strongest signal, there is a ~7 μm and ~14 μm shift in focus for the Gaussian and annular illumination, respectively, when the 780 nm wavelength illumination is changed to 950 nm. The comparatively slower defocusing of the annular beam can be attributed to the longer axial extent of the Bessel-Gauss beam formed at the focus. Finally, only a 4.19 ± 0.48% difference in the measured PSF values for the RO is observed.

Table 4.1. Summary of TPF PSF measurements and collagen fiber size calculations from SHG images taken with SO and RO

TPF imaging of fluorescent beads				SHG Imaging of tendon			
$\lambda_{EXC}/\lambda_{EM}$ (nm)	Average experimental PSF (nm)		Average % Δ PSF	% Difference in fiber sizes			Average % Difference
	780/530	950/530		ΔA	ΔB	ΔC	
SO - Gaussian	750.40 ± 44.34	1068.60 ± 49.24	42.62± 7.01	11.32	12.13	12.21	11.89±0.49
SO - Annular	750.80 ± 76.34	947.40 ± 102.89	26.14± 4.08	10.18	9.66	11.09	10.31±0.72
RO - Annular	772.80 ± 15.86	805.20 ± 15.57	4.19 ± 0.48	3.23	4.48	3.87	3.86±0.63

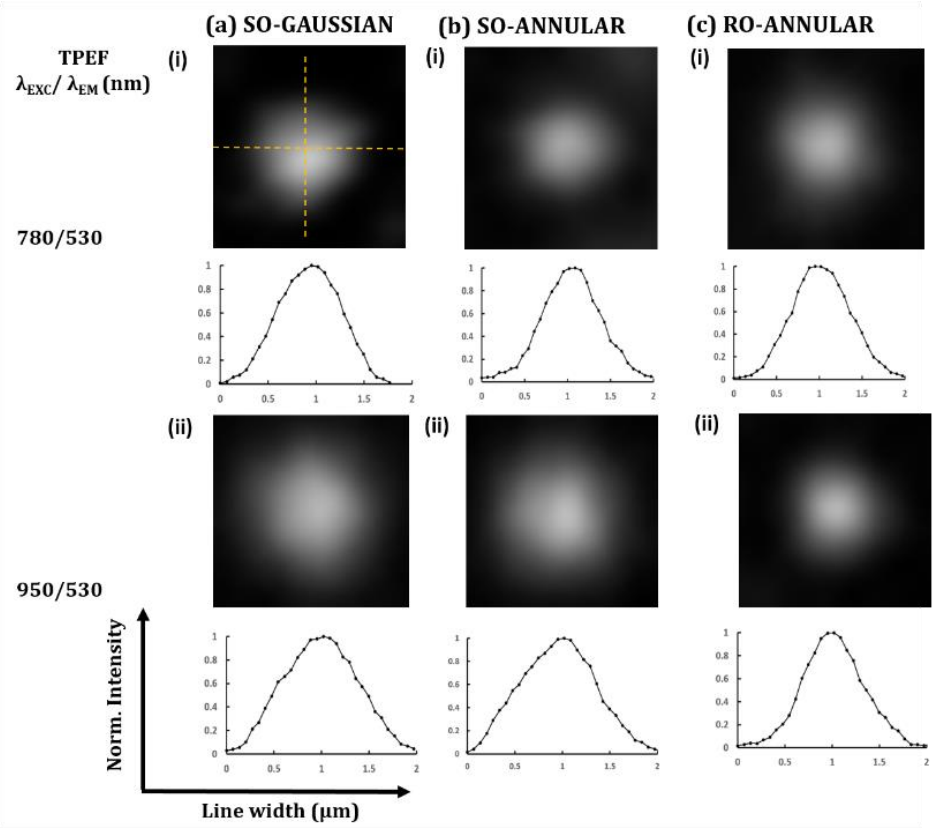

Fig. 4.3: Comparison of TPF PSF of fluorescent beads using various (a-c) objective and illumination combinations. For each combination, (i) 780 and (ii) 950 nm excitation wavelengths were considered. Line intensity profiles are obtained along horizontal and vertical directions, shown by yellow dashed lines in (a,i). Horizontal line intensity profiles for each bead is shown below the image of the bead. See text for details. Adapted from Kabir et al. with permission [86].

Considering the results obtained from TPF imaging, it would be useful to note the utility of using the RO in multimodal MPM imaging where different nonlinear processes need distinct input wavelengths of light. For example, SHG images of breast tissue would depict the structure of the collagen fiber network [87], whereas THG images obtained at the same location would present the distribution of various types of cellular structures in that plane [88]. To ensure that the third-

harmonic emission wavelength is contained within the spectral window of standard point detectors, the illumination wavelength in THG imaging has been shifted further into NIR compared to that used in SHG imaging. However, THG typically needs tighter focusing than SHG, so the moderate NA of the RO may lead to THG images with significantly reduced SNR. Despite the availability of ROs with higher NA (0.65), their application to imaging has led to undesired geometric aberrations [71]. To illustrate the advantage of using an RO over a wide wavelength range, SHG imaging is performed using 780 and 950 nm illumination, with 390 and 475 nm as emission wavelengths, the results of which are presented in Fig. 4.4 for the 25 μm thick porcine tendon tissue used as the sample for this experiment. For the SHG images obtained with the SO utilizing a Gaussian and an annular beam (Fig. 4.4a and b), a shift in the focal plane is observed between images (i) and (ii) which leads to fibers appearing sharp at one wavelength, blurred at the other wavelength, or even not appearing at all. From these images, we measure collagen fiber widths at three different locations marked with A, B and C in the images obtained with 780 nm illumination [Fig. 4.4a(i), b(i) and c(i)] and corresponding locations marked with A', B' and C' in images taken with 950 nm illumination [Fig. 4.4a(ii), b(ii) and c(ii), depicted by yellow lines]. Subsequently, the percentage difference in fiber widths for each location is calculated and the average percentage difference along with standard deviation is also obtained. A summary of these results is presented in columns 5 – 8 of Table 4.1. We observe 11.89±0.49 % and 10.31±0.72% differences in fiber widths on average for the SO using a Gaussian and an annular illumination, respectively. The lower difference in feature sizes due to chromatic dispersion compared to the TPF results can be ascribed to the larger sizes of the collagen fibers compared to fluorescent beads. This factor leads to less severe defocusing error. In contrast, a similar set of measurements performed with the RO yields an average of 3.86±0.62% changes in fiber widths [Fig. 4.4(c)]. This result is consistent with that obtained from TPF images.

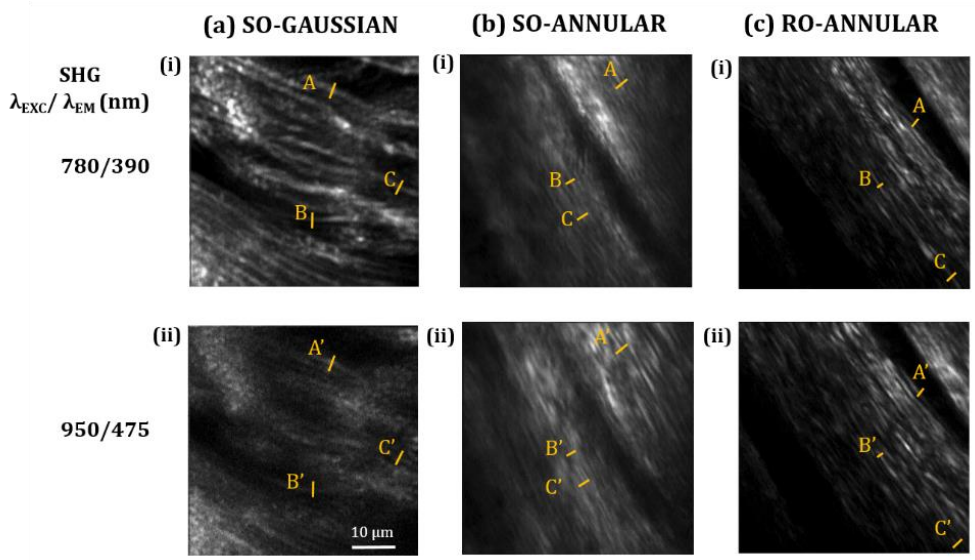

Fig. 4.4: Comparison of SHG images taken with various (a–c) objective and illumination combinations. For each combination, two different excitation wavelengths (780 and 950 nm) are shown (i and ii). Intensity profile for fiber width measurements were drawn along the yellow line segments indicated in each figure. Adapted from Kabir et al. [86] with permission.

Despite their utility in reducing chromatic aberration, ROs currently suffer several limitations to their applicability in MPM imaging. In a backward signal collection mechanism, neither the TPF nor the SHG signal is generated with an annular intensity distribution. This factor leads to a portion of the emitted signal being blocked by the aperture stop of the RO during signal collection, thereby reducing the signal collection efficiency. For SHG imaging, this factor reduces the effectiveness of the RO when imaging randomly organized, and/or sparsely distributed samples that typically produce comparatively weaker signals. To that end, we chose a densely packed, well-aligned porcine tendon tissue for SHG imaging which contains a coherent organization of spatially concentrated second-order nonlinearity.

4.4 Conclusion

In summary, TPF and SHG microscopy were utilized to compare the performance of a 0.5-NA reflective objective with a 0.55-NA standard glass objective, using focused Gaussian and Bessel beam illumination. Using illumination and detection wavelengths within the visible and NIR, the use of the SO leads to defocusing errors of ~25–40% for TPF images of sub-diffraction fluorescent beads, and ~10-12% errors for SHG images of collagen fibers. A ~4% defocusing error was obtained for the RO using both imaging modalities. This work underscores the potential of ROs for simultaneous wavelength viewing in multimodal MPM applications with Bessel beam illumination.

Chapter 5

APPLICATION OF A UNIFORM ILLUMINATION INTENSITY FOR MULTIPHOTON MICROSCOPY

5.1 Background

To meet the requirement of temporal and spatial simultaneity of *n* photons for an *n*-photon excitation process, common hardware implementations of MPM utilize respectively, ultrafast optical pulses (typically ~100 fs) and a tight point-focused beam (achieved by a high-numerical-aperture objective lens). Point-focused illumination requires that the beam is scanned across the surface of the sample and the emitted signal from each illuminated spot is serially collected by a point detector to construct a 2D image. Despite the ability to obtain a sub-micrometer spatial resolution, the point-scanning scheme can have several limitations. Firstly, the requirement of serial point-scanning makes this method inherently slower than widefield illumination, i.e., illuminating the complete region of interest with a single beam. Secondly, the focal field intensity distribution is proportional to an 'Airy-disk' function [44, 58] which has a non-uniform intensity distribution. As individual multiphoton processes occur within a region smaller than the focal volume, the generated signal may have a larger contribution from particles at the center of the volume than those at the periphery. This factor requires that the neighboring

scanned points be overlapped in an effort to compensate for the lack of illumination uniformity. This oversampling of scanned points increases the number of scanning steps, further constraining the image acquisition speed. Various approaches have been adopted to increase the imaging throughput, one of which focuses on using mirrors with increased scanning speeds (~ 160 µs/line) [89, 90]. However, this approach has an upper limit based on the speed of the fastest scanning mirrors and the highest repetition rate of short-pulsed laser sources. Relatively higher frame rates of up to 30 kHz have been observed in TPF [91] and THG microscopy [92] by generating a line focus with cylindrical optics and scanning the line along a single dimension in the sample plane. Other researchers have explored the conditions necessary for widefield image acquisition, i.e., illuminating the region of interest and subsequently acquiring the image in a single frame [93-96]. By utilizing a comparatively higher illumination power, widefield imaging has been successfully demonstrated for TPF and SHG microscopy [95, 97, 98] and combined with digital holography [96] for 3D image reconstruction.

In a conventional widefield imaging system the intensity distribution of the illumination beam is Gaussian. This results in only a segment at the center of the beam having sufficient intensity to generate a detectable multiphoton effect whereas power in the edge of the beam is wasted. The beam power can be increased to ensure multiphoton interaction within a larger area of the beam, but this will mean that the SNR at various locations in the image would not only depend on the sample, but also on the illumination intensity distribution [99]. As such, the obtained image may not be a true representation of the structural construction the sample, leading to erroneous results in any intensity dependent quantitative analysis. In addition, increasing the beam power raises the possibility of photon induced damage such as phototoxicity or bleaching of fluorophores. In that respect, flat-top beams (FTB), i.e., beams with a uniform spatial intensity distribution, can help mitigate some of these problems. In recent times FTBs have been widely adapted in various linear microscopy techniques to obtain illumination field homogenization. In its simplest form a rotating diffuser [100] has been used to

obtain a time-averaged speckle pattern of approximately uniform intensity distribution to improve the accuracy in single molecule localization. This method was later improved by incorporating a pair of microlens arrays [101] at the expense of moving components in the optical setup, which may lead to unwanted vibration in the imaging system. Time-averaging also constrains the imaging speed with respect to the speed of the spinning device. More importantly, the loss of coherence as light travels through the diffuser impedes the adoption of these techniques to coherent multiphoton processes such as SHG and THG. Another widely prevalent method for generating FTB involves the use of diffractive beam-shapers [102-105], which redistributes the illumination intensity by interfering various diffracted orders. These diffraction effects are accurate within a narrow wavelength bandwidth which limits the usage of these devices in multimodal MPM platforms that require multiple illumination wavelengths [86]. Diffractive optics also create undesired diffraction orders, and their efficiency is strongly dependent on manufacturing tolerances. Alternatively, refractive phase elements have been used to redistribute the illumination Gaussian beam (GB) to FTBs with ~95% power throughput and ~2.5% inhomogeneity in the intensity distribution. Recently, one such beam shaper has been used to increase the accuracy of single molecule localization for a super-resolution microscope [99]. In this paper we utilize a refractive Gaussian-to-top-hat beam shaper to generate a square-shaped FTB, and compare its performance with that of a standard GB for a widefield MPM imaging system. In particular, we characterize the effect of adopting a square-shaped uniform intensity distribution on the image contrast and quantitative image analysis for TPF and SHG imaging. We begin by simulating the effect of beam diameter and beam power on the intensity distribution of GBs and compare the beam power distribution with that of an FTB. Subsequently, we compare the 2D spatial distribution of the SNR obtained from TPF images of a uniform layer of fluorescent dye using a widefield GB (WF-GB) and a widefield FTB (WF-FTB) illumination mode. Next, we demonstrate the applicability of the FTB for biological tissue imaging by capturing TPF and SHG images of various biological tissues. We

then demonstrate the effect of reduced illuminated area caused by a GB illumination on quantitative orientation analysis of obtained SHG images. Finally, we demonstrate the more general applicability of WF-FTB illumination for another multiphoton application, namely two-photon absorption induced polymerization (TPP). Section 5.2 provides the methods, whereas section 5.3 provides the results and discussion. Finally section 5.4 provides the conclusion.

5.2 Methods

5.2.1 Sample preparation

Fluorescein dyes, *Convallaria* and mouse colon tissue were used for TPF, whereas chicken tendon and human breast tissue biopsy samples were used for SHG imaging in this study. Unstained *Convallaria majalis* (lily-of-the-valley) sample was purchased from MSMedia (New South Wales, Australia). The sample contained an array of two 1 mm sections of *Convallaria* tissue which were fixed and mounted between a cover slip and a microscope slide. Each section has a thickness of 30 µm. Mouse colon tissue was obtained locally from an abattoir and placed in tissue cassettes (Fisher Scientific). Next, it was processed in a standard xylene/ethanol mixture for 24 hours for extensive dehydration. The sample was then embedded in paraffin wax using a tissue processor (Leica ASP300). Next, 8 µm thick sections were cut using a cryostat (Leica CM3050S) and stained with hematoxylene and eosin (H&E) stain. Finally, each tissue section was mounted onto a microscope slide with a permanent mounting media (Permount).

Chicken tendon tissues were collected from a local abattoir and preserved in an embedding medium at -80 °C. Next, the samples were slowly raised to a temperature of -20 °C and 5 µm thick sections were cut using a cryostat (Leica CM3050S). Subsequently, the samples were thawed and stained with hematoxylene and eosin (H&E) stain. Finally, the tissue section was mounted onto a microscope slide with a permanent mounting media (Permount).

A tissue microarray of breast tissue biopsy was purchased from US Biomax (Rockville, MD, USA). The microarray consists of 1.5 mm diameter cores which are formalin-fixed and paraffin-embedded breast tissue samples. The samples include H&E stained 5 μm thick invasive ductal carcinoma tissue paired with normal breast tissue samples mounted on a microscope slide.

TPP was performed with a photocurable polymer, which was prepared from a mixture of 98 ml Poly(ethylene glycol) diacrylate (Sigma-Aldrich, CAS 26570-48-9), 2g Phenylbis (2,4,6-trimethylbenzoyl)phosphine oxide (Sigma-Aldrich, CAS 162881-26-7) and 0.02 g Sudan I (Sigma-Aldrich, CAS 842-07-9). To form a homogeneous mixture, all chemical components were mixed 24 hours prior to usage, and stored in a dark glass bottle to isolate the solution from ambient light. A drop of the mixture was placed on a microscope slide and covered with a cover slip to form a thin layer of the photopolymer.

5.2.2 Mathematical model of the flat-top beam

The expression for the optical field of an FTB with a square cross section can be modeled as [106-108]

$$U_l\ x,y\ = E_0 g(\tfrac{x}{r_i},\tfrac{y}{r_i})\exp[i\beta\varphi(\tfrac{x}{r_i},\tfrac{y}{r_i})], \tag{5.1}$$

where E_0 is the amplitude, $g(\frac{x}{r_i},\frac{y}{r_i})$ is the shape function of the incident beam, $\varphi(\frac{x}{r_i},\frac{y}{r_i})$ is the phase factor required to generate the FTB, and β is scaling factor expressed as

$$\beta = \tfrac{\pi\omega_0 R_o}{f\lambda}, \tag{5.2}$$

where ω_o, R_o, f, and λ refer to the incident Gaussian beam diameter, width of the FTB, focal length of the focusing lens, and wavelength of the beam, respectively. For an input GB, the incident field distribution can be described as

$$g\ \xi\ = \exp\Big(-\tfrac{\xi^2}{2}\Big) \tag{5.3}$$

where $\xi = (\frac{2\sqrt{2}x}{\omega_0}, \frac{2\sqrt{2}y}{\omega_0})$. The aforementioned phase factor φ can be expressed as

$$\varphi\ \xi\ = \frac{\pi}{2}\xi \mathrm{erf}\ \xi\ + \frac{1}{2}\exp\ -\xi^2\ - \frac{1}{2}, \tag{5.4}$$

where 'erf' describes the error function. An ideal FTB is defined with an infinite intensity gradient at its edges which is obtained when $\beta \to \infty$.

5.2.3 Experimental setup

Figure 5.1 shows the custom-built MPM setup used in this study. An ultrafast titanium:sapphire pulsed laser (Spectra-Physics Mai-Tai HP, Santa Clara, CA, USA) is used to generate a Gaussian beam with 100 fs pulses at a repetition rate of 80 MHz. The laser is spectrally tunable between 690 and 1050 nm and the excitation wavelength for this study is spectrally centered at 780 nm. An optical spatial filter is used to isolate the fundamental Gaussian mode and enlarge the beam diameter to 5 mm. A half-wave plate and a polarizer are used together to control the power of the beam. Next, a pair of metallic mirrors reflect the beam onto the back aperture of a Gaussian-to-top-hat beam shaper lens (TOPAG Lasertechnik GmbH, GTH-5-250-4-NIR, Darmstadt, Germany). The beam shaper redistributes the 5 mm diameter Gaussian beam into square-shaped 4x4 mm flat-top beam (FTB) at a distance of 250 mm. We use Zemax (OpticStudio, Kirkland, WA, USA) to simulate the propagation of the illumination beam through the beam shaper and visualize the resulting spatial intensity distribution of the FTB. To perform this simulation, a 3D model of the beam shaper is obtained from the vendor (TOPAG Lasertechnik GmbH, Darmstadt, Germany). The inset in Fig. 5.1 shows the normalized (a) 2D and (b) 1D intensity distribution of the FTB. We observe that the normalized root mean square value of the FTB is 0.92 for the flat region bounded by the white square shown in the 2D intensity profile. Beyond this region, the intensity decreases with a sharp gradient (shown by shaded blue areas).

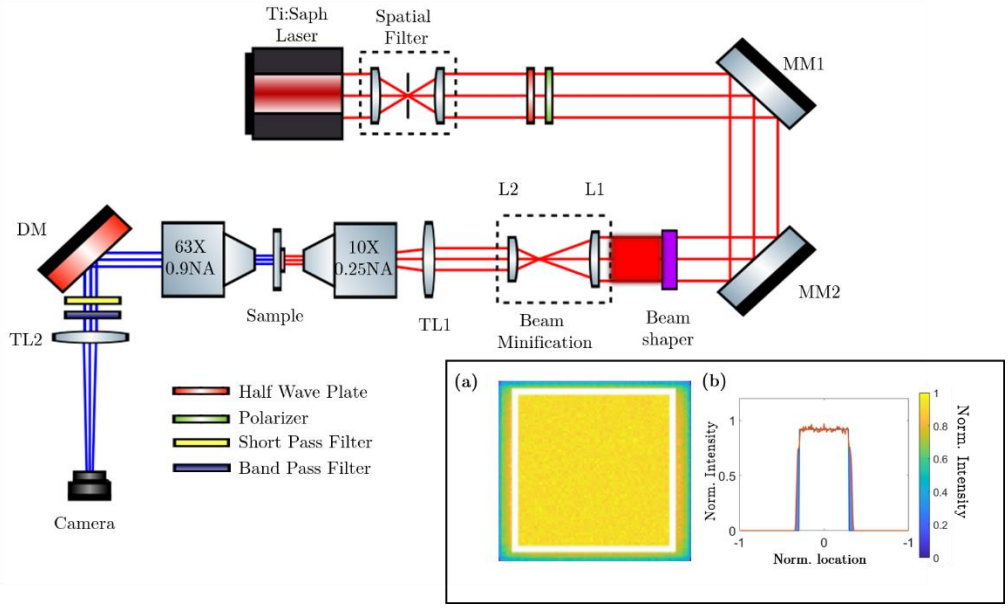

Fig. 5.1: Schematic diagram of the experimental setup showing a modified MPM incorporating a square-shaped flat-top beam illumination. Inset shows the simulated 2D and 1D intensity distribution of the FTB. MM1 and MM2: metal mirrors, TL1 and TL2: tube lens, DM: dichroic mirror.

After the generation of the FTB, a pair of convex lenses (f1 = 10 cm, f2 = 5 cm) is used to minify the FTB to a size of 2x2 mm and relay the FTB on to the image plane of a tube lens TL1 (f3 = 40 cm). From the tube lens, the beam is passed onto a 0.25 numerical aperture (NA), 10× objective lens (Olympus America, Model, USA) which relays the FTB on to the sample plane. The size of the FTB at the sample plane is 60x60 µm. To obtain a GB illumination, the beam shaper is simply removed from the beam path which leads to an illumination spot size of diameter 60 µm at the sample plane. Note that a beam average power of ~600 mW is required to obtain TPF and SHG images for both beams for a widefield illumination condition. A brief discussion about the power requirements for a widefield SHG imaging system is presented in Appendix A. Both forward propagating TPF and SHG signals are collected using a 0.9 NA condenser lens (Carl Zeiss Microscopy, Condsr Achr Apl 0.9 H D Ph DIC). The emitted signals

are reflected by a dichroic mirror onto a laser-blocking filter (Semrock FF01-680/SP-25, Rochester, NY, USA) and a relevant bandpass filter (Semrock FF01-530/40-25 for TPF, Semrock FF01- 390/18-25 for SHG, Rochester, NY, USA). Finally, the emitted signal is focused on to an EMCCD camera (Hamamatsu EM-CCD C9100-13, Bridgewater, NJ, USA) with the help of tube lens TL2 (f4 = 30 cm). An image acquisition time of 1.5 seconds is utilized for all imaging modes.

5.3 Results and Discussion

We begin our study by comparing the theoretical power distribution for various cases of GBs and the FTB, the results of which are shown in Fig. 5.2. Using custom-written Matlab (Mathworks, Natick, MA) code, we simulate the illumination intensity distribution for three different cases of the GBs over an arbitrary square area of 2x2 units. For all cases, a 2D illumination intensity distribution is obtained, and the corresponding 1-dimensional (1D) line intensity profile calculated along the x-axis (horizontal green line in Fig. 5.2a) is shown below the 2D plots. The intensity values are plotted on a normalized scale and a value of 0.5 is chosen as an intensity detection threshold for two-photon processes (shown by a black line in the 1D line intensity profiles). For each beam, the power is obtained by calculating the area under the intensity profile. The threshold is defined as the intensity value below which no detectable two-photon signal is obtained. Note that for the EMCCD camera used in this study this detection threshold corresponds to the noise floor dictated by the photon shot noise and the quantum efficiency of the device, which is ~55% at a wavelength of 390 nm and ~90% at a wavelength of 530 nm. The white rectangle in Fig. 5.2 denotes the imaging area. As shown in columns (a - c), the three GBs are chosen based on beam diameter and power, whereby the red circle shows the size of the GB corresponding to the intensity threshold. For the first case of the GB shown in column (a), the diameter of the

beam, defined by its full width at half maximum (FWHM), is chosen to be 0.75 units, and the maximum intensity value is normalized to 1. For this GB, we observe that 51.9% of the beam power reaches the threshold (white rectangular area) and is optimally used for two-photon processes. We also note that 23.35% of the beam power is above the threshold (shown in red shaded area) leading to a significant beam overexposure to the sample. We also observe that 24.75% of the beam power is below the two-photon intensity threshold (shown in blue shaded areas). With an aim to reduce the power distributed in overexposure, we consider a second case of the GB as shown in column (b), where the beam diameter is kept fixed but the total power is reduced to 60% of its previous value. In this case, overexposure is reduced significantly to 2.53% of the total beam power which is also depicted by the reduced red region in the 1D line intensity profile. However, a larger portion of the beam amounting to 55.26% falls below the intensity threshold as indicated by the larger blue shaded area and as such is not utilized for the two-photon process. Only 42.21% of the beam power reaches the two-photon threshold. For the final case of the GB shown in column (c), we consider an enlarged GB beam where the diameter is 1.25x larger than the GB considered in the first case. The total beam power is kept constant, which leads to a reduction of the maximum intensity by ~25%. In this case, 18.45% of the beam power contributes to overexposure, whereas 32.85% of the beam power falls below the intensity threshold and does not contribute to the two-photon process. The portion of the beam power which is optimally utilized amounts to 48.7% for this case. Finally, column (d) shows the 2D and 1D intensity distribution for a square-shaped FTB which is obtained utilizing the mathematical formulation for the FTB depicted in the Methods section. For an incident Gaussian beam diameter of 5 mm, FTB width of 4 mm, incident wavelength of 780 nm and focal length of the focusing lens of 250 mm, we evaluate the value of β to be 645 as defined by Eqn. (5.2) of the Methods section. For the purpose of comparison, the width of the FTB is chosen to be equal to the diameter of the GB in the first case (0.75 units) and its intensity is chosen to be equal to the two-photon intensity threshold. From the 2D and 1D intensity

profiles shown in Fig. 5.2(c), we observe that a negligible part of the beam is under-utilized or distributed in overexposure. The corresponding values for overexposure, underexposure and optimum utilization are 1.77%, 9.14% and 89.09% respectively for the square-shaped FTB obtained by simulating the beam propagation through the beam shaper. From the results of this study summarized in Table 5.1, it is obvious that a uniform intensity distribution leads to a significant increase in the utilization of the beam power for two-photon processes.

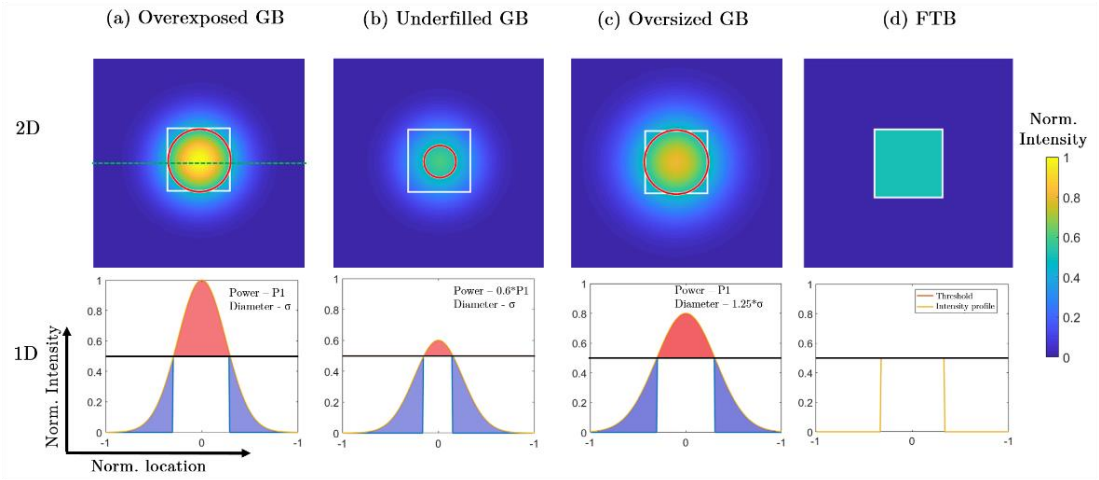

Fig. 5.2: Comparison of the illumination intensity distribution of GB and FTB. Simulated 2D transverse (*x-y*) intensity distributions are plotted for an (a) overexposed, (b) underfilled and (c) overfilled GB and compared with a (d) FTB. The white rectangle defines the imaging area and the red circles denote the diameter of the GB that corresponds to the intensity threshold. Dimensions for all 2D plots are 2x2 arbitrary units. As shown by the green dashed line in (a), line intensity profiles are obtained along the horizontal direction and they are shown below the 2D intensity plots. Overexposed regions are shaded in pink, whereas underexposed regions are shaded in blue. See text for details.

Table 5.1: Comparison of the power distribution in GBs and FTBs

	Overexposed GB	Underfilled GB	Oversized GB	Theoretical FTB	Simulated FTB
% Over-exposed	23.35	2.53	14.37	0	1.77
% Under-Exposed	24.75	55.26	37.64	0	9.14
% Optimally Utilized	51.9	55.26	48.7	100	89.09

Next, we compare the distribution of SNR on TPF images of a uniform layer of fluorescent dyes using a widefield Gaussian beam (WF-GB) and a widefield flat top beam (WF-FTB) illumination systems, the results of which are shown in Fig. 5.3(i and ii), respectively. Column (a) depicts the TPF images, where we clearly notice the disparity in intensity distribution between these two beams. From these images, we calculate the SNR for each point within the image and develop a 2D SNR map as shown in column (b). The noise value in the SNR map is obtained by calculating the average intensity of a 25x25 pixel region in an image captured in the camera without the presence of the illumination beam. From the 2D TPF SNR map for the WF-GB shown in (b,i) we observe a significant variation in SNR between the periphery and the center of the image, whereas the corresponding 2D TPF SNR map for WF-FTB shown in (b,ii) demonstrates only a modest variation in its SNR distribution. These results are further clarified by observing the 1D SNR variation along the x- and y-axis shown in columns (c) and (d), respectively. To obtain the 1D SNR distribution along the x-axis we define a horizontal rectangular region of 5x60 µm for both 2D SNR maps as shown in column (b), and plot the average SNR values within that region. A similar procedure is adopted for the 1D SNR distribution along the y-axis, whereby the average SNR values obtained from a 60x5 µm vertical rectangle are plotted. As shown in (c,i) and (d,i), the SNR variation between the edge and center of the image for WF-GB is 6.59 and 6.62 dB along the x- and y-axes, respectively. The corresponding variation for

the WF-FTB shown in (c,ii) and (d,ii) is 1.32 dB for both the x- and y-axes, respectively.

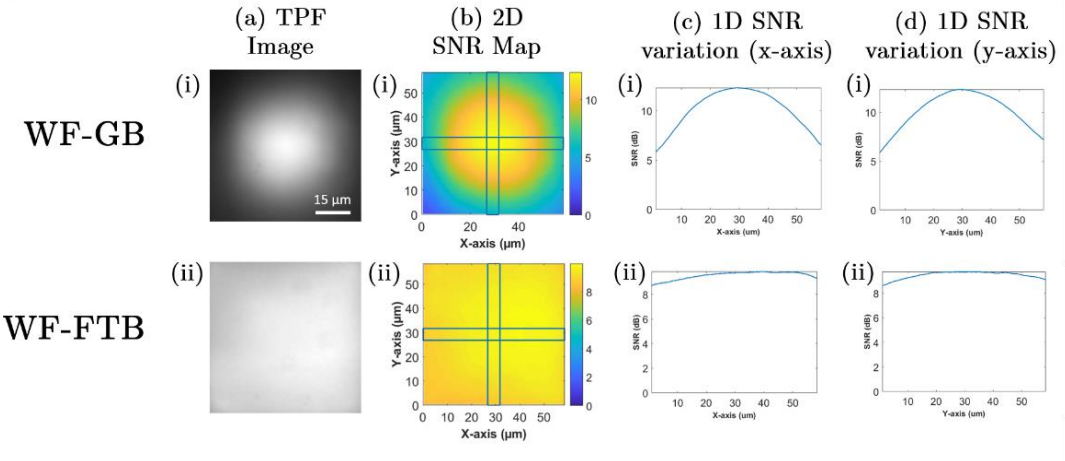

Fig. 5.3: Comparison of the SNR distribution in TPF images. (i) WF-GB and (ii) WF-FTB illumination is used to obtain (a) TPF images of a uniform layer of fluorescent dye. For each case, the corresponding (b) 2D and 1D SNR distribution along the (c) x- and (d) y-axis is demonstrated.

Next, we apply the WF-FTB imaging platform to obtain TPF and SHG images of biological tissues and compare the illumination of the region of interest in the imaging plane with a WF-GB imaging modality. Four different tissue types were chosen showing biological structures of varying shapes and sizes. As shown in Fig. 5.4, mouse colon and *Convallaria* rhizome tissue are chosen for TPF imaging, whereas chicken tendon and human breast biopsy tissue are chosen for SHG imaging. The TPF images of the colon shown in Fig. 5.4(a) showcase a collection of immune cells, whereas Fig. 5.4(b) depicts a cross-section of the *Convallaria* rhizome. In both cases, WF-GB shows lack of illumination in the corners of the image which results in several immune cells in the colon and some portion of the *Convallaria* vascular boundaries appearing with a poor contrast or not appearing at all. We also note a strong background signal in Fig. 5.4(a,i) which is significantly reduced in Fig. 5.4(a,ii). As the GB is overexposed towards the center, a stronger

out-of-plane signal is detected in the WF-GB modality, which contributes to the stronger background signal. Figure 5.4(c) and (d) show similar effects of reduced illumination in SHG images of tendon and breast biopsy. Tendon has thicker, densely packed, uniformly oriented collection of collagen fibers, whereas the fibers in the breast tissue are comparatively more fragmented, sparsely distributed and randomly oriented. Despite these differences, both sets of images show observable lack of illumination at the corners and overexposed contrast near the center of the image in images taken with WF-GB modality. By comparing 10 sets of images taken with WF-GB and WF-FTB illumination for each type of tissue, we observe that the images obtained with WF-GB showcases ~ 20% more dark area than images taken with WF-FTB.

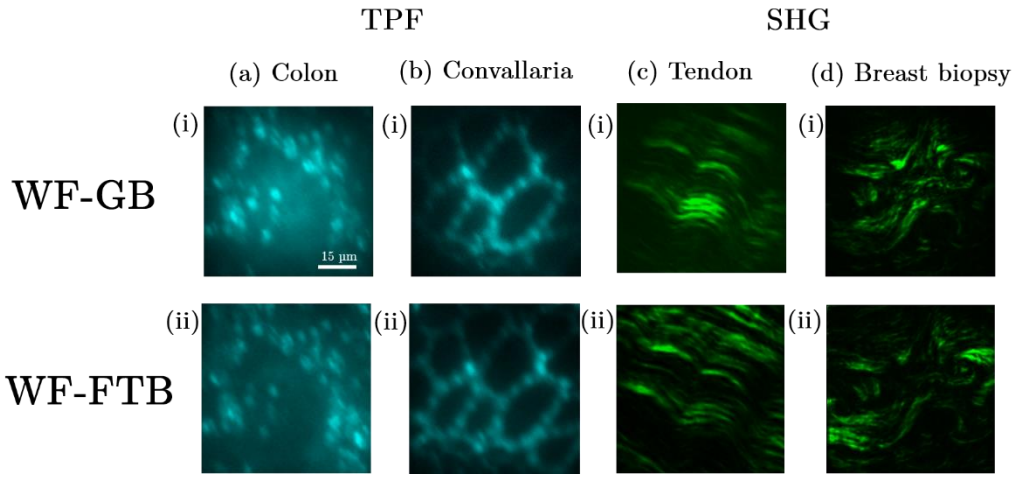

Fig. 5.4: Application of FTB in WF-MPM imaging of biological tissues. TPF images of (colon) and (b) *convallaria* roots, and SHG images of (c) chicken tendon and (d) human breast biopsy are obtained using (i) WF-GB and (ii) WF-FTB imaging platforms.

The aforementioned vignetting has the potential to change the results of quantitative image analysis performed with a WF-GB as the intensity values will not be a true representation of the structure. More specifically, any feature located near the corners of an image will not be included in the analysis, which can lead to erroneous evaluation of the structural content of the whole image. To elucidate this factor, we applied 2D Fourier transform-based orientation analysis (FT-SHG)

on SHG images of breast biopsy tissue, the results of which are shown in Fig. 5.5. The details of this analysis technique are presented elsewhere [10]. Briefly, we divide the images into 18x18 grids, where each grid has a dimension of 8x8 pixels. For an image dimension of 60x60 μm, this results in 324 grids. If the average intensity within each grid is below a pre-defined noise threshold, the grid is labeled as a dark region and overlaid with a cyan color. Next, the variation in fiber orientation within each grid is used to define it as an anisotropic or an isotropic region, whereby it is overlaid with a magenta color in the latter case. Finally, the preferred orientation of fibers within each anisotropic grid is calculated and displayed. By comparing the results of this analysis, we observe from Fig. 5.5(a) that the image taken with WF-GB contains significantly more dark regions compared to the image taken with WF-FTB. From the bar plot summarizing the number of dark, anisotropic and isotropic regions shown in Fig. 5.5(b), we observe that 127 more grids are marked as dark in the image captured with WF-GB, which reduces the number of isotropic and anisotropic regions by 25 and 102, respectively. These discrepancies lead to differences in the orientation analysis, which is depicted in the circular histograms shown in Fig. 5.5(c). We observe that the preferred orientation of fibers is 19.8° for the SHG image taken with WF-GB whereas the value is 22.4° for the image obtained with WF-FTB. The distribution of fiber orientation between anisotropic grids is depicted by the circular variance, which assumes values of 0.165 and 0.229 for images taken with WF-GB and WF-FTB imaging modalities, respectively. We attribute this discrepancy to the fact that ~20% more area is considered for orientation analysis in the WF-FTB image.

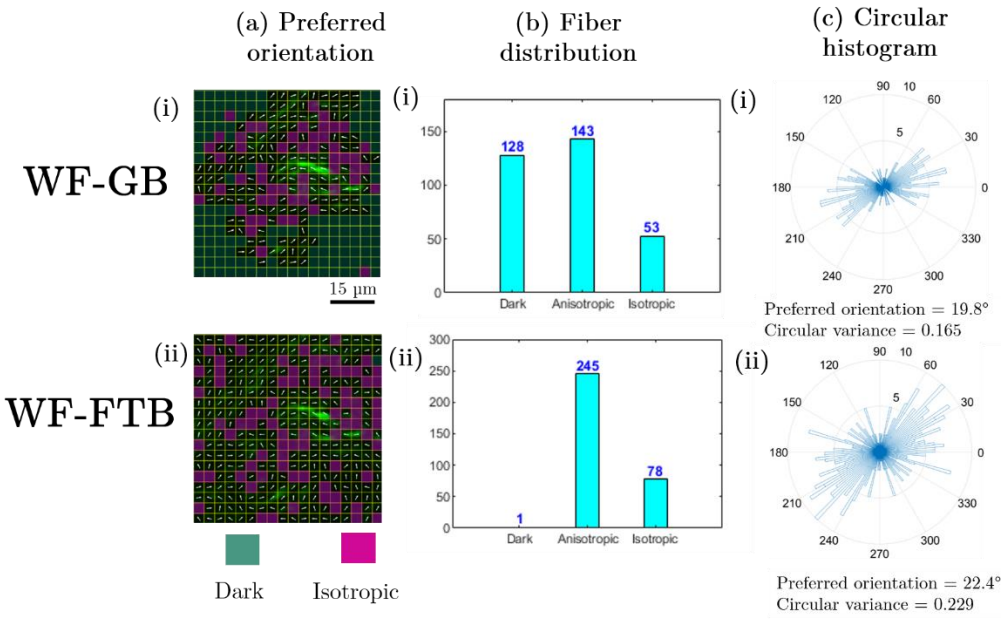

Fig. 5.5: Effect of illumination distribution on orientation analysis of SHG images. FT-SHG analysis was applied to obtain (a) preferred orientation of collagen fibers in SHG images of breast biopsy tissue obtained with (i) WF-GB and (ii) WF-FTB illumination. (b) The bar plot demonstrates the number of dark, anisotropic and isotropic regions, whereas a (c) circular histogram shows the distribution of fiber orientation within the anisotropic regions.

The WF-FTB illumination can also be adapted to additive manufacturing applications based on multiphoton processes. TPP is one such method, which uses a point-scanning laser beam to perform maskless direct laser lithography that enables fabrication of sub-micron scale structures for applications in optical communication [109], biological sensing [110] and MEMS devices [110, 111]. In TPP, two-photon absorption in the resin leads to cross-linking and polymerization, which results in fabrication of the structure. Since the fidelity of the structure manufactured depends on the two-photon absorption process, TPP is fundamentally governed and limited by principles very similar to those of TPF microscopy. Hence, we expect that using a WF-FTB in TPP would lead to similar advantages, such as simultaneous polymerization of the complete desired

manufacturing area in a photosensitive resin and a uniform polymerization rate across the whole illuminated region. These two factors would potentially ensure minimal undesired variations in the structures manufactured. To demonstrate this advantage, we perform TPP with a WF-FTB and compare the results with a WF-GB illumination, the results of which are shown in Fig. 5.6. The illumination configuration shown in the experimental setup in Fig. 5.1 was adapted for this process. For both illumination conditions, the photosensitive resin is exposed to a beam of ~580 mW average power for a duration of 30 seconds, to ensure the average intensity is sufficient for complete polymerization. Using a WF-GB illumination, we observe that only the central area is polymerized, where the intensity of light is higher than the polymerization threshold of the resin. As the intensity decreases from the center towards the edge, the manufactured structure loses its integrity and becomes ill-formed. In contrast, we observe a comparatively uniform structure with sharply defined boundaries when WF-FTB was used for the manufacturing process. This observation suggests uniform and complete polymerization throughout the entire illuminated area.

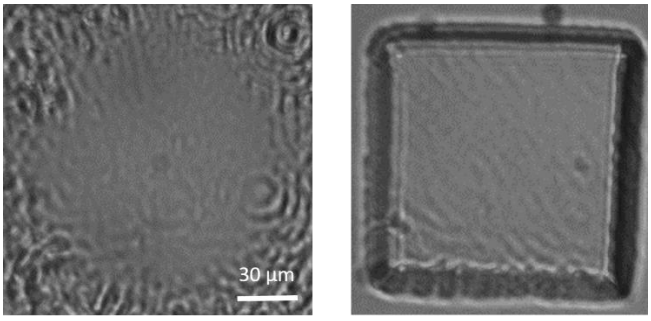

Fig. 5.6: Two-photon polymerization using (a) WF-GB, and (b) WF-FTB illumination. See text for details.

Notwithstanding the applicability of WF-FTB illumination for multiphoton imaging and manufacturing applications, some limitations should be considered for its full implementation. Due to the use of a low NA objective lens to create the widefield illumination, the axial extent of the beam is on the order of tens of

microns. This factor leads to a reduced axial resolution and hampers the formation of 3D images. Computational reconstruction techniques such as digital holography can be used to mitigate some of these issues by recovering 3D structural information from SHG images [96].

5.4 Conclusion

In summary, we utilized a square-shaped flat-top beam to perform multiphoton microscopy and polymerization under widefield illumination conditions. Compared to a WF-GB illumination, the use of a WF-FTB provides ~40% more optimal utilization of beam power in two-photon imaging applications. From TPF imaging of fluorescent dye, we observed a 5.6 and 1.2 dB difference in SNR between the edge and the center of the beam for WF-GB and WF-FTB illumination profiles, respectively. Moreover, we found ~20% more dark areas in TPF images of mouse colon and Convallaria, and SHG images of chicken tendon and human breast biopsy tissue obtained with a WF-GB modality. The potential effect of reduced illuminated area in quantitative orientation analysis of collagen fibers was demonstrated by a ~4% difference in fiber orientation and ~7% difference in circular variance in SHG images of breast biopsy tissue. In addition, WF-FTB illumination was also found to be effective for multiphoton additive manufacturing which was demonstrated by an increased polymerization uniformity in a two-photon polymerization process. Our work highlights the various potential benefits from considering FTB as an illumination modality for multiphoton applications.

CHAPTER 6

CONCLUSION AND FUTURE DIRECTIONS

6.1 Summary of Current Work

This dissertation presents the work done to incorporate focal field beam shaping in nonlinear two-photon microscopy. In particular, two different illumination intensity profiles are adopted and their performance is characterized with respect to the current state of the art. The first approach utilizes a mirror-based reflective microscope objective (RO) and a Bessel-Gauss (B-G) beam illumination to mitigate chromatic aberration in TPF and SHG imaging. The performance of the RO-based imaging system was systematically compared to the conventional imaging system that uses glass-based standard microscope objectives (SO). Experiments traversing ~ 1 octave in the visible and near infrared wavelengths, showcase a chromatic aberration of 25-40% for TPF images of fluorescent beads obtained with the SO, whereas the corresponding defocusing errors were 10-12% for SHG images of collagen fibers in tendon. In both cases, ~4% error was observed for the RO. This work underlines the potential utility of ROs for multimodal multiphoton microscopy.

The second research work adopts a widefield imaging configuration with a uniform illumination intensity distribution to reduce intensity-based vignetting. The conventional widefield microscope utilizes a Gaussian beam which has a non-uniform intensity distribution. By adopting a square-shaped flat-top beam (FTB)

to obtain the uniform illumination, the probability of multiphoton effects is equalized throughout the imaging area. Compared to a widefield Gaussian beam (WF-GB) illumination, the widefield FTB (WF-FTB) provides ~4.4 dB reduction in the difference of SNR between the edge and the center of the image. TPF images of mouse colon and plant convallaria, and SHG images of chicken tendon and human breast biopsy tissue showcase ~25% more dark area for the WF-GB imaging modality. The increased dark area can influence quantitative analysis which is indicated by up to ~4% difference in fiber orientation and ~4% difference in circular variance observed in orientation analysis of collagen fibers in SHG images of breast biopsy tissue. This study presents WF-FTB as a suitable illumination platform for quantitative SHG imaging of fast, dynamic biological processes.

6.2 Future Directions

As mentioned in Chapter 2, the point-scanning system is the most prevalent method used in SHG microscopy. In this method an 'Airy-disk' intensity profile is formed at the focal plane of the focusing objective, leading to a non-uniform illumination intensity distribution. To ensure that the SHG image is a true representation of the nonlinear process throughout the imaging area, the scanning points need to be oversampled. Oversampling increases the image acquisition time and places a temporal constraint on the speed of the biological processes that can be captured. Adopting an FTB for the point-scanning system can help mitigate this problem. The first step would be to determine the appropriate technique for generating an FTB that ensures minimal distortion when focused by a high NA objective lens. A simpler starting point could be to adopt a flattened-Gaussian beam (FGB) which is a class of beams with a circular 2D cross section and uniform illumination intensity. Appendix B provides a brief discussion about FGBs and suitable techniques to generate them. The next step would entail the characterization of the experimentally obtained intensity distribution, which would highlight any intensity distortion and indicate the lateral dimensions of the FTB.

Based on the lateral dimensions, the beam scanning steps can be determined to obtain an optimum scanning speed.

In addition to the beam shapes already adopted, a wide variety of other intensity distributions have the potential to be adopted for SHG microscopy. Airy beam is one such beam form which demonstrates a non-diffracting intensity profile [112]. A relatively wider transverse intensity spread has led to the use of an Airy beam in single photon light sheet microscopy, where it has shown four- and tenfold increase in the illumination field-of-view compared to Bessel-Gauss and Gaussian light sheet illumination, respectively [113]. As such, it will be useful to characterize the performance of an Airy beam in a multiphoton imaging system, especially when compared to the performance obtained by the conventional illumination beams.

Finally, it is pertinent to note that different beam shapes lead to the optimization of different parameters in the SHG microscope. For example, a Bessel-Gauss beam is useful in the fast measurement of the collagen content in a 3D volume of a certain tissue sample. To that end, it will be useful to develop an information database summarizing the characteristics of each beam form, a suitable generation technique, the particular optimization that it brings to the imaging system and the quantitative metric that benefits from its adoption. This database will be immensely helpful for both researchers and biologists to determine the suitable beam shape for their particular application.

APPENDIX A

WIDEFIELD ILLUMINATION PARAMETERS

To obtain an understanding of the improvement in imaging throughput by widefield illumination, it is useful to compare the imaging conditions of such a system with that of a point scanning system. In a typical SHG imaging process, the number of second-harmonic photons generated per unit illuminated area is defined as [114]

$$N \propto |\chi^{(2)}|^2 \frac{E_p^2}{\tau A} f, \tag{A.1}$$

where E_p is the pulse energy of the beam, $\chi^{(2)}$ is the second-order nonlinear susceptibility, τ is the pulsewidth, f is the repetition rate and A is the area of the illuminated spot. For an imaging system with n scanning points, increasing the illumination area to the whole imaging area leads to a decrease in the number of generated photons by n. However, the SHG signal could be restored to its previous level by increasing the pulse energy by $\sqrt{n}$ times. As the pulse energy is proportional to the beam power, this would mean increasing the power by $\sqrt{n}$ times.

APPENDIX B

FLATTENED-GAUSSIAN BEAM

An FGB of order N and beam spot size w_0 can be expressed by the following field distribution [115]:

$$\mathrm{E}\ r, z=0\ = E_0 \exp(-\tfrac{(N+1)r^2}{w_0^2}) \sum_{m=0}^{N}\ \tfrac{1}{m!}(\tfrac{(N+1)r}{w_0})^m, \tag{B.1}$$

where r denotes the radial coordinate and E_0 is the complex factor. As mentioned earlier, such a beam assumes a Gaussian form for $N = 0$ and approaches $E_0 \mathrm{circ}(r/w_0)$ when N approaches ∞. Figure B.1(a) shows the 2D intensity distribution that corresponds to an FGB with $N = 100$. A comparison of the transverse intensity distribution for FGBs is shown for two different orders ($N = 1 \text{ and } 100$) in Fig. B.1(b). The field of Eqn. (B.1) can be expressed as the finite sum of Laguerre-Gaussian beams as [116]

$$E\ r, z=0\ = E_0 \sum_{n=0}^{N}\ c_n L_n(\tfrac{2(N+1)r^2}{w_0^2}) \exp(-\tfrac{(N+1)r^2}{w_0^2}), \tag{B.2}$$

where $c_n = (-1)^n \sum_{m=n}^{N} \binom{m}{n} \frac{1}{2^m}$ and L_n is the *n*th Laguerre polynomial. Hence, the propagation of a FGB under paraxial condition can be expressed as

$$\begin{aligned} E\ r\ = E_0 \tfrac{\omega_N\ 0}{\omega_N\ 0} \exp\{i[kz - \varphi_N\ z\ ]\} \\ \times \exp\left\{\left[\frac{ik}{2R_N\ z} - \frac{1}{{\omega_N}^2\ z}\right] r^2\right\} \\ \times \sum_{n=0}^{N} {c_n}^N\ L_n[\tfrac{2r^2}{{\omega_N}^2\ z}] \exp[-2in\varphi_N(z)], \end{aligned} \tag{B.3}$$

where k is the wave number, and ω_N, R_N, and φ_N are denoted by

$$\omega_N\ z\ = \omega_N(0)\sqrt{1 + [\tfrac{\lambda z}{\pi {\omega_N}^2\ 0}]^2}, \tag{B.4a}$$

$$R_N\ z\ = z(1+\left[\frac{\pi\omega_N{}^2\ 0}{\lambda z}\right]^2), \tag{B.4b}$$

$$\varphi_N\ z\ = \arctan[\frac{\lambda z}{\pi\omega_N{}^2\ 0}]. \tag{B.4c}$$

The spot size of the FGB $\omega_N\ 0$ is related to the Gaussian beam waist as $\omega_N\ z\ = \omega_0/\sqrt{N+1}$. It should be noted that the transverse profile loses its uniform distribution after propagation. This happens due to the dephasing of the individual components of the Laguerre-Gaussian beams.

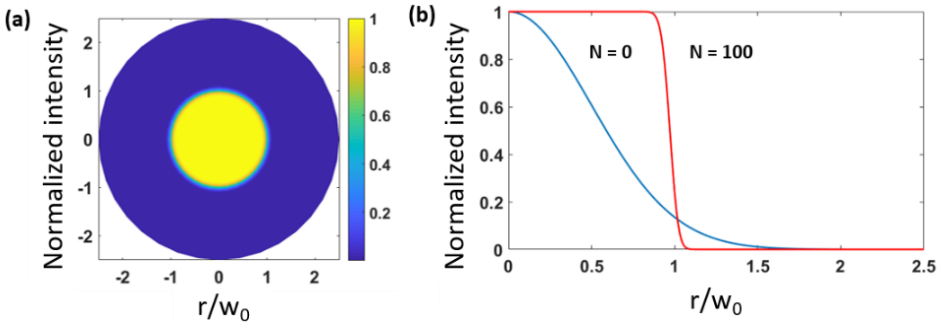

Fig. B.1. Normalized intensity distribution of an FGB, depicted in (a) 2D ($N = 100$) and (b) 1D.

A suitable approach for generating a FGB can be developed by observing the far-field propagation profile of the FGB. It is observed that the in the far-field Fraunhofer regime [116] an FGB field is transformed into a 'Jinc' function, and the intensity profile assumes an Airy disk pattern expressed by Eqn. (B.1). By invoking Fourier transform properties of the objective lens, a collimated beam with an Airy disk pattern could be transformed to an FGB at the focus of the lens.

REFERENCES

[1] P. A. Franken, A. E. Hill, C. W. Peters, and G. Weinreich, "Generation of optical harmonics," *Physical Review Letters,* vol. 7, no. 4, pp. 118-119, 08/15/ 1961.

[2] S. Tokutake, Y. Imanishi, and M. Sisido, "Efficiency of second harmonic generation from amino acids, peptides, and polypeptides carrying polarizable aromatic groups," *Molecular Crystals and Liquid Crystals,* vol. 170, no. 1, pp. 245-257, 1989.

[3] R. Hellwarth and P. Christensen, "Nonlinear optical microscopic examination of structure in polycrystalline ZnSe," *Optics Communications,* vol. 12, no. 3, pp. 318-322, 1974.

[4] J. N. Gannaway and C. J. R. Sheppard, "Second-harmonic imaging in the scanning optical microscope," *Optical and Quantum Electronics,* vol. 10, no. 5, pp. 435-439, 1978/09/01 1978.

[5] S. Fine and W. Hansen, "Optical second harmonic generation in biological systems," *Applied optics,* vol. 10, no. 10, pp. 2350-2353, 1971.

[6] I. Freund and M. Deutsch, "Second-harmonic microscopy of biological tissue," *Optics Letters,* vol. 11, no. 2, pp. 94-96, 1986/02/01 1986.

[7] P. P. Provenzano, K. W. Eliceiri, J. M. Campbell, D. R. Inman, J. G. White, and P. J. Keely, "Collagen reorganization at the tumor-stromal interface facilitates local invasion," *BMC Medicine,* vol. 4, 2006, Art. no. 38.

[8] R. Ambekar, T. Y. Lau, M. Walsh, R. Bhargava, and K. C. Toussaint Jr, "Quantifying collagen structure in breast biopsies using second-harmonic generation imaging," *Biomedical Optics Express,* vol. 3, no. 9, pp. 2021-2035, 2012.

[9] W. Lo *et al.*, "Intact corneal stroma visualization of GFP mouse revealed by multiphoton imaging," *Microscopy Research and Technique,* vol. 69, no. 12, pp. 973-975, 2006.

[10] R. A. R. Rao, M. R. Mehta, and K. C. Toussaint, "Fourier transform-second-harmonic generation imaging of biological tissues," *Optics Express,* vol. 17, no. 17, pp. 14534-14542, 2009.

[11] S.-J. Lin *et al.*, "Discrimination of basal cell carcinoma from normal dermal stroma by quantitative multiphoton imaging," *Optics Letters,* vol. 31, no. 18, pp. 2756-2758, 2006.

[12] S.-P. Tai *et al.*, "Optical biopsy of fixed human skin with backward-collected optical harmonics signals," *Optics Express,* vol. 13, no. 20, pp. 8231-8242, 2005.

[13] W. Lee, M. H. Rahman, M. E. Kersh, and K. C. Toussaint, "Application of quantitative second-harmonic generation microscopy to posterior cruciate ligament for crimp analysis studies," *Journal of Biomedical Optics,* vol. 22, no. 4, p. 046009, 2017.

[14] T. Y. Lau, R. Ambekar, and K. C. Toussaint, "Quantification of collagen fiber organization using three-dimensional Fourier transform-second-harmonic generation imaging," *Optics Express,* vol. 20, no. 19, pp. 21821-21832, 2012.

[15] M. Sivaguru *et al.*, "Quantitative analysis of collagen fiber organization in injured tendons using Fourier transform-second harmonic generation imaging," *Optics Express,* vol. 18, no. 24, pp. 24983-24993, 2010.

[16] R. Ambekar, M. Chittenden, I. Jasiuk, and K. C. Toussaint Jr, "Quantitative second-harmonic generation microscopy for imaging porcine cortical bone: comparison to SEM and its potential to investigate age-related changes," *Bone,* vol. 50, no. 3, pp. 643-650, 2012.

[17] T. Lau, H. Sangha, E. Chien, B. McFarlin, A. Wagoner Johnson, and K. Toussaint, "Application of Fourier transform-second-harmonic generation imaging to the rat cervix," *Journal of Microscopy,* vol. 251, no. 1, pp. 77-83, 2013.

[18] M. M. Kabir, V. K. Inavalli, T.-Y. Lau, and K. C. Toussaint, "Application of quantitative second-harmonic generation microscopy to dynamic conditions," *Biomedical Optics Express,* vol. 4, no. 11, pp. 2546-2554, 2013.

[19] M. M. Kabir, A. Jonayat, S. Patel, and K. C. Toussaint, "Graphics processing unit-based quantitative second-harmonic generation imaging," *Journal of Biomedical Optics,* vol. 19, no. 9, p. 096009, 2014.

[20] M. Sivaguru *et al.*, "Application of an advanced maximum likelihood estimation restoration method for enhanced-resolution and contrast in second-harmonic generation microscopy," *Journal of Microscopy,* vol. 267, no. 3, pp. 397-408, 2017.

[21] X. Chen, O. Nadiarynkh, S. Plotnikov, and P. J Campagnola, "Second harmonic generation microscopy for quantitative analysis of collagen fibrillar structure," *Nature Protocols,* vol. 7, no. 4, pp. 654-69, 2012.

[22] C. Okoro and K. C. Toussaint, "Experimental demonstration of two-photon Mueller matrix second-harmonic generation microscopy," *Journal of Biomedical Optics,* vol. 21, no. 1, p. 016011, 2016.

[23] J. V. Thompson, B. H. Hokr, G. A. Throckmorton, D. Wang, M. O. Scully, and V. V. Yakovlev, "Enhanced second harmonic generation efficiency via wavefront shaping," *ACS Photonics,* vol. 4, no. 7, pp. 1790-1796, 2017.

[24] N. Tian, L. Fu, and M. Gu, "Resolution and contrast enhancement of subtractive second harmonic generation microscopy with a circularly polarized vortex beam," *Scientific Reports,* vol. 5, p. 13580, 2015.

[25] T. V. Truong, W. Supatto, D. S. Koos, J. M. Choi, and S. E. Fraser, "Deep and fast live imaging with two-photon scanned light-sheet microscopy," *Nature Methods,* vol. 8, no. 9, p. 757, 2011.

[26] N. Vuillemin *et al.*, "Efficient second-harmonic imaging of collagen in histological slides using Bessel beam excitation," *Scientific Reports,* vol. 6, p. 29863, 2016.

[27] R. O. Hynes, "The extracellular matrix: not just pretty fibrils," *Science,* vol. 326, no. 5957, pp. 1216-1219, 2009.

[28] R. O. Hynes and A. Naba, "Overview of the matrisome—an inventory of extracellular matrix constituents and functions," *Cold Spring Harbor Perspectives in Biology,* vol. 4, no. 1, p. a004903, 2012.

[29] P. Fratzl, *Collagen: Structure and Mechanics*. Springer Science & Business Media, 2008.

[30] G. Scarr, "Simple geometry in complex organisms," *Journal of Bodywork and Movement Therapies,* vol. 14, no. 4, pp. 424-444, 2010.

[31] K. Gelse, E. Pöschl, and T. Aigner, "Collagens—structure, function, and biosynthesis," *Advanced Drug Delivery Reviews,* vol. 55, no. 12, pp. 1531-1546, 2003.

[32] S. M. Weis, J. L. Emery, K. D. Becker, D. J. McBride Jr, J. H. Omens, and A. D. McCulloch, "Myocardial mechanics and collagen structure in the osteogenesis imperfecta murine (oim)," *Circulation Research,* vol. 87, no. 8, pp. 663-669, 2000.

[33] F. Rauch and F. H. Glorieux, "Osteogenesis imperfecta," *The Lancet,* vol. 363, no. 9418, pp. 1377-1385, 2004.

[34] D. J. Maitland and J. T. Walsh Jr, "Quantitative measurements of linear birefringence during heating of native collagen," *Lasers in Surgery and Medicine: The Official Journal of the American Society for Laser Medicine and Surgery,* vol. 20, no. 3, pp. 310-318, 1997.

[35] M. C. Pierce, R. L. Sheridan, B. H. Park, B. Cense, and J. F. de Boer, "Collagen denaturation can be quantified in burned human skin using polarization-sensitive optical coherence tomography," *Burns,* vol. 30, no. 6, pp. 511-517, 2004.

[36] M. Wolman and F. Kasten, "Polarized light microscopy in the study of the molecular structure of collagen and reticulin," *Histochemistry,* vol. 85, no. 1, pp. 41-49, 1986.

[37] S. L. Jacques, J. R. Roman, and K. Lee, "Imaging superficial tissues with polarized light," *Lasers in Surgery and Medicine: The Official Journal of the American Society for Laser Medicine and Surgery,* vol. 26, no. 2, pp. 119-129, 2000.

[38] A. Changoor *et al.*, "Structural characteristics of the collagen network in human normal, degraded and repair articular cartilages observed in polarized light and scanning electron microscopies," *Osteoarthritis and Cartilage,* vol. 19, no. 12, pp. 1458-1468, 2011.

[39] T. Starborg *et al.*, "Using transmission electron microscopy and 3View to determine collagen fibril size and three-dimensional organization," *Nature protocols,* vol. 8, no. 7, p. 1433, 2013.

[40] W. Lee and K. C. Toussaint, "Quantitative second-harmonic generation imaging of tissue damage from environmental-scanning electron microscopy," in *Frontiers in Optics*, 2018, p. JTu2A. 119: Optical Society of America.

[41] A. Young, I. J. Legrice, M. A. Young, and B. Smaill, "Extended confocal microscopy of myocardial laminae and collagen network," in *Journal of Microscopy,* vol. 192, no. 2, pp. 139-50, 1998.

[42] S. M Warren, B. Walder, W. Dec, M. T Longaker, and K. Ting, "Confocal laser scanning microscopic analysis of collagen scaffolding patterns in cranial sutures," in *The Journal of Craniofacial Surgery,* vol. 19, no. 1, pp. 198-203, 2008.

[43] L. Mastropasqua *et al.*, "Morphological modification of the cornea after standard and transepithelial corneal cross-linking as imaged by anterior segment optical coherence tomography and laser scanning in vivo confocal microscopy," in *Cornea,* vol. 32, no. 6, pp. 855-861, 2013.

[44] M. C. Teich, and B. E. Saleh, *Fundamentals of Photonics*. Wiley New York, 1991.

[45] M. Göppert-Mayer, "Über elementarakte mit zwei quantensprüngen," *Annalen der Physik,* vol. 401, no. 3, pp. 273-294, 1931.

[46] W. Mohler, A. C. Millard, and P. J. Campagnola, "Second harmonic generation imaging of endogenous structural proteins," *Methods,* vol. 29, no. 1, pp. 97-109, 2003.

[47] R. W. Boyd, *Nonlinear Optics*. Academic Press, 2003.

[48] I. V. Shadrivov, A. A. Zharov, and Y. S. Kivshar, "Second-harmonic generation in nonlinear left-handed metamaterials," *JOSA B,* vol. 23, no. 3, pp. 529-534, 2006.

[49] T. Kowalczyk, K. Singer, and P. Cahill, "Anomalous-dispersion phase-matched second-harmonic generation in a polymer waveguide," *Optics Letters,* vol. 20, no. 22, pp. 2273-2275, 1995.

[50] M. Hobden, "Phase-matched second-harmonic generation in biaxial crystals," *Journal of Applied Physics,* vol. 38, no. 11, pp. 4365-4372, 1967.

[51] N. Dong, F. Chen, and J. Vázquez de Aldana, "Efficient second harmonic generation by birefringent phase matching in femtosecond-laser-inscribed KTP cladding waveguides," *Physica Status Solidi (RRL)–Rapid Research Letters,* vol. 6, no. 7, pp. 306-308, 2012.

[52] M. Yamada, N. Nada, M. Saitoh, and K. Watanabe, "First-order quasi-phase matched $LiNbO_3$ waveguide periodically poled by applying an external field for efficient blue second-harmonic generation," *Applied Physics Letters,* vol. 62, no. 5, pp. 435-436, 1993.

[53] P. S. Kuo, J. Bravo-Abad, and G. S. Solomon, "Second-harmonic generation using-quasi-phasematching in a GaAs whispering-gallery-mode microcavity," *Nature Communications,* vol. 5, p. 3109, 2014.

[54] R. LaComb, O. Nadiarnykh, and P. J. Campagnola, "Quantitative second harmonic generation imaging of the diseased state osteogenesis imperfecta: experiment and simulation," *Biophysical Journal,* vol. 94, no. 11, pp. 4504-4514, 6/1/ 2008.

[55] B. R. Masters and P. So, *Handbook of Biomedical Nonlinear Optical Microscopy*. Oxford University Press, 2008.

[56] L. Moreaux, O. Sandre, and J. Mertz, "Membrane imaging by second-harmonic generation microscopy," *JOSA B,* vol. 17, no. 10, pp. 1685-1694, 2000.

[57] J. B. Pawley, *Handbook of Biological Confocal Microscopy*. Springer London, Limited, 1995.

[58] J. W. Goodman, *Introduction to Fourier Optics*. W. H. Freeman, 2005.

[59] W. R. Zipfel, R. M. Williams, R. Christiet, A. Y. Nikitin, B. T. Hyman, and W. W. Webb, "Live tissue intrinsic emission microscopy using multiphoton-excited native fluorescence and second harmonic generation," *Proceedings of the National Academy of Sciences of the United States of America,* vol. 100, no. 12, pp. 7075-7080, 2003.

[60] C. Okoro and K. C. Toussaint, "Second-harmonic patterned polarization-analyzed reflection confocal microscope," *Journal of Biomedical Optics,* vol. 22, no. 8, pp. 086007, 2017.

[61] Y. Wang, C. M. Oh, M. C. Oliveira, M. S. Islam, A. Ortega, and B. H. Park, "GPU accelerated real-time multi-functional spectral-domain optical coherence tomography system at 1300nm," *Optics Express,* vol. 20, no. 14, pp. 14797-14813, 2012.

[62] N. H. Cho *et al.*, "High speed SD-OCT system using GPU accelerated mode for in vivo human eye imaging," *Journal of the Optical Society of Korea,* vol. 17, no. 1, pp. 68-72, 2013.

[63] J. Li, P. Bloch, J. Xu, M. V. Sarunic, and L. Shannon, "Performance and scalability of Fourier domain optical coherence tomography acceleration using graphics processing units," *Applied Optics,* vol. 50, no. 13, pp. 1832-1838, 2011.

[64] M. Shneider, A. Voronin, and A. Zheltikov, "Action-potential-encoded second-harmonic generation as an ultrafast local probe for nonintrusive membrane diagnostics," *Physical Review E,* vol. 81, no. 3, p. 031926, 2010.

[65] W. Richardson, "Bayesian-based iterative method of image restoration," *Journal of the Optical Society of America A,* vol. 62, no. 1, pp. 55-59, 1972.

[66] L. B. Lucy, "An iterative technique for the rectification of observed distributions," *The Astronomical Journal,* vol. 79, no. 6, pp. 745, 1974.

[67] A. Goldraij *et al.*, "Compartmentalization of S-RNase and HT-B degradation in self-incompatible Nicotiana," *Nature,* vol. 439, no. 7078, pp. 805, 2006.

[68] M. Sivaguru, L. Mander, G. Fried, and S. W. Punyasena, "Capturing the surface texture and shape of pollen: a comparison of microscopy techniques," *PloS One,* vol. 7, no. 6, pp. 39129, 2012.

[69] H. Segawa, M. Okuno, H. Kano, P. Leproux, V. Couderc, and H.-o. Hamaguchi, "Label-free tetra-modal molecular imaging of living cells with CARS, SHG, THG and TSFG (coherent anti-Stokes Raman scattering, second harmonic generation, third harmonic generation and third-order sum frequency generation)," *Optics Express,* vol. 20, no. 9, pp. 9551-9557, 2012.

[70] C. Burch, "Reflecting microscopes," *Proceedings of the Physical Society,* vol. 59, no. 1, pp. 41, 1947.

[71] D. S. Grey and P. H. Lee, "A new series of microscope objectives: I. Catadioptric Newtonian systems," *Journal of the Optical Society of America A,* vol. 39, no. 9, pp. 719-722, 1949.

[72] R. Barer, A. Cole, and H. Thompson, "Infra-red spectroscopy with the reflecting microscope in physics, chemistry and biology," *Nature,* vol. 163, no. 4136, pp. 198-201, 1949.

[73] V. Raghunathan, Y. Han, O. Korth, N.-H. Ge, and E. O. Potma, "Rapid vibrational imaging with sum frequency generation microscopy," *Optics Letters,* vol. 36, no. 19, pp. 3891-3893, 2011.

[74] C. Schmidt *et al.*, "Multi-order investigation of the nonlinear susceptibility tensors of individual nanoparticles," *Scientific Reports,* vol. 6, pp. 25415, 2016.

[75] D. Vucinic, T. M. Bartol Jr, and T. J. Sejnowski, "Hybrid reflecting objectives for functional multiphoton microscopy in turbid media," *Optics Letters,* vol. 31, no. 16, pp. 2447-2449, 2006.

[76] C. A. Combs *et al.*, "Compact non-contact total emission detection for in vivo multiphoton excitation microscopy," *Journal of Microscopy,* vol. 253, no. 2, pp. 83-92, 2014.

[77] H. Inagawa, Y. Toratani, K. Motohashi, I. Nakamura, M. Matsushita, and S. Fujiyoshi, "Reflecting microscope system with a 0.99 numerical aperture designed for three-dimensional fluorescence imaging of individual molecules at cryogenic temperatures," *Scientific Reports,* vol. 5, 2015.

[78] B. Amirsolaimani, B. Cromey, N. Peyghambarian, and K. Kieu, "All-reflective multiphoton microscope," *Optics Express,* vol. 25, no. 19, pp. 23399-23407, 2017.

[79] J. Durnin, J. Miceli Jr, and J. Eberly, "Diffraction-free beams," *Physical Review Letters,* vol. 58, no. 15, p. 1499, 1987.

[80] E. Botcherby, R. Juškaitis, and T. Wilson, "Scanning two photon fluorescence microscopy with extended depth of field," *Optics Communications,* vol. 268, no. 2, pp. 253-260, 2006.

[81] G. Thériault, M. Cottet, A. Castonguay, N. McCarthy, and Y. De Koninck, "Extended two-photon microscopy in live samples with Bessel beams: steadier focus, faster volume scans, and simpler stereoscopic imaging," *Frontiers in Cellular Neuroscience,* vol. 8, pp. 139, 2014.

[82] P. Vaity and L. Rusch, "Perfect vortex beam: Fourier transformation of a Bessel beam," *Optics Letters,* vol. 40, no. 4, pp. 597-600, 2015.

[83] A. T. Friberg, "Stationary-phase analysis of generalized axicons," *Journal of the Optical Society of America A,* vol. 13, no. 4, pp. 743-750, 1996.

[84] J. H. McLeod, "The axicon: a new type of optical element," *Journal of the Optical Society of America A,* vol. 44, no. 8, pp. 592-597, 1954.

[85] G. Indebetouw, "Nondiffracting optical fields: some remarks on their analysis and synthesis," *Journal of the Optical Society of America A,* vol. 6, no. 1, pp. 150-152, 1989.

[86] M. M. Kabir, A. M. Choubal, and K. C. Toussaint Jr, "Application of a reflective microscope objective for multiphoton microscopy," *Journal of Microscopy,* vol. 271, no. 2, pp. 129-135, 2018.

[87] R. Ambekar, T.-Y. Lau, M. Walsh, R. Bhargava, and K. C. Toussaint, "Quantifying collagen structure in breast biopsies using second-harmonic generation imaging," *Biomedical Optics Express,* vol. 3, no. 9, pp. 2021-2035, 2012.

[88] W. Lee, M. M. Kabir, R. Emmadi, and K. C. Toussaint, "Third-harmonic generation imaging of breast tissue biopsies," *Journal of Microscopy,* vol. 264, no. 2, pp. 175-181, 2016.

[89] K. H. Kim, C. Buehler, and P. T. So, "High-speed, two-photon scanning microscope," *Applied Optics,* vol. 38, no. 28, pp. 6004-6009, 1999.

[90] V. Iyer *et al.*, "Acousto-optic multiphoton laser scanning microscopy (AO-MPLSM) for structural and functional imaging in living brain slices," in *Multiphoton Microscopy in the Biomedical Sciences V*, 2005, vol. 5700, pp. 90-102: International Society for Optics and Photonics.

[91] G. Brakenhoff, J. Squier, T. Norris, A. C. Bliton, M. Wade, and B. Athey, "Real-time two-photon confocal microscopy using a femtosecond, amplified Ti: sapphire system," *Journal of Microscopy,* vol. 181, no. 3, pp. 253-259, 1996.

[92] D. Oron and Y. Silberberg, "Third-harmonic generation with cylindrical Gaussian beams," *Journal of the Optical Society of America B,* vol. 21, no. 11, pp. 1964-1968, 2004.

[93] M. Sonnleitner, G. Schütz, and T. Schmidt, "Imaging individual molecules by two-photon excitation," *Chemical Physics Letters,* vol. 300, no. 1-2, pp. 221-226, 1999.

[94] D. N. Fittinghoff, P. W. Wiseman, and J. A. Squier, "Widefield multiphoton and temporally decorrelated multifocal multiphoton microscopy," *Optics Express,* vol. 7, no. 8, pp. 273-279, 2000.

[95] L.-C. Cheng *et al.*, "Spatiotemporal focusing-based widefield multiphoton microscopy for fast optical sectioning," *Optics Express,* vol. 20, no. 8, pp. 8939-8948, 2012.

[96] O. Masihzadeh, P. Schlup, and R. A. Bartels, "Label-free second harmonic generation holographic microscopy of biological specimens," *Optics Express,* vol. 18, no. 10, pp. 9840-9851, 2010.

[97] C. Macias-Romero *et al.*, "High throughput second harmonic imaging for label-free biological applications," *Optics Express,* vol. 22, no. 25, pp. 31102-31112, 2014.

[98] C. Macias-Romero, I. Nahalka, H. I. Okur, and S. Roke, "Optical imaging of surface chemistry and dynamics in confinement," *Science,* vol. 357, no. 6353, pp. 784-788, 2017.

[99] C. J. Rowlands, F. Ströhl, P. P. V. Ramirez, K. M. Scherer, and C. F. Kaminski, "Flat-field super-resolution localization microscopy with a low-cost refractive beam-shaping element," *Scientific Reports,* vol. 8, no. 1, p. 5630, 2018.

[100] H. Ma, R. Fu, J. Xu, and Y. Liu, "A simple and cost-effective setup for super-resolution localization microscopy," *Scientific Reports,* vol. 7, no. 1, p. 1542, 2017.

[101] K. M. Douglass, C. Sieben, A. Archetti, A. Lambert, and S. Manley, "Super-resolution imaging of multiple cells by optimized flat-field epi-illumination," *Nature Photonics,* vol. 10, no. 11, pp. 705, 2016.

[102] W. Veldkamp, "Laser beam profile shaping with interlaced binary diffraction gratings," *Applied Optics,* vol. 21, no. 17, pp. 3209-3212, 1982.

[103] X. G. Huang, M. R. Wang, and C. Yu, "High-efficiency flat-top beam shaper fabricated by a nonlithographic technique," *Optical Engineering,* vol. 38, no. 2, 1999.

[104] H. Kiriyama *et al.*, "High-spatiotemporal-quality petawatt-class laser system," *Applied Optics,* vol. 49, no. 11, pp. 2105-2115, 2010.

[105] G. Račiukaitis *et al.*, "Laser processing by using diffractive optical laser beam shaping technique," *Journal of Laser Micro/nanoengineering,* vol. 6, no. 1, 2011.

[106] C. C. Aleksoff, K. K. Ellis, and B. D. Neagle, "Holographic conversion of a Gaussian beam to a near-field uniform beam," *Optical Engineering,* vol. 30, no. 5, pp. 537-544, 1991.

[107] F. M. Dickey and S. C. Holswade, "Gaussian laser beam profile shaping," *Optical Engineering,* vol. 35, no. 11, pp. 3285-3296, 1996.

[108] L. Romero and F. Dickey, "Lossless laser beam shaping," *Journal of the Optical Soceity of America A,* vol. 13, no. 4, pp. 751-760, 1996.

[109] M. Deubel, G. Von Freymann, M. Wegener, S. Pereira, K. Busch, and C. M. Soukoulis, "Direct laser writing of three-dimensional photonic-crystal templates for telecommunications," *Nature Materials,* vol. 3, no. 7, p. 444, 2004.

[110] C. Accoto *et al.*, "Two-photon polymerization lithography and laser Doppler vibrometry of a SU-8-based suspended microchannel resonator," *Journal of Microelectromechanical Systems,* vol. 24, no. 4, pp. 1038-1042, 2015.

[111] B. H. Cumpston *et al.*, "Two-photon polymerization initiators for three-dimensional optical data storage and microfabrication," *Nature,* vol. 398, no. 6722, p. 51, 1999.

[112] G. A. Siviloglou, J. Broky, A. Dogariu, and D. N. Christodoulides, "Observation of accelerating Airy beams," *Physical Review Letters,* vol. 99, no. 21, pp. 213901, 2007.

[113] T. Vettenburg *et al.*, "Light-sheet microscopy using an Airy beam," *Nature Methods,* vol. 11, no. 5, pp. 541, 2014.

[114] J. Dadap, X. Hu, M. Russell, J. Ekerdt, J. Lowell, and M. Downer, "Analysis of second-harmonic generation by unamplified, high-repetition-rate, ultrashort laser pulses at Si (001) interfaces," *IEEE Journal of Selected Topics in Quantum Electronics,* vol. 1, no. 4, pp. 1145-1155, 1995.

[115] F. Gori, "Flattened Gaussian beams," *Optics Communications,* vol. 107, no. 5-6, pp. 335-341, 1994.

[116] V. Bagini *et al.*, "Propagation of axially symmetric flattened Gaussian beams," *Journal of the Optical Society of America A,* vol. 13, no. 7, pp. 1385-1394, 1996.